ELSEVIER

On the relationship between surface pressure, terrain elevation, and air temperature. Part I: The large diurnal surface pressure range at Gale Crater, Mars and its origin due to lateral hydrostatic adjustment

Mark I. Richardson [*], Claire E. Newman

Aeolis Research, Pasadena, CA, USA

A B S T R A C T

The daily variation of surface pressure observed by the Curiosity Rover Environmental Monitoring Station (REMS) is both significantly larger than observed at other landing sites on Mars and larger than simulated for the Curiosity site by global circulation models (GCM). Mesoscale numerical models are able to simulate the large REMS daily pressure range, but only if they possess sufficiently high horizontal resolution (grid spacing <5 km); low resolution (120–500 km) GCM simulations typically generate daily ranges of about half the observed value. The pressure range in low resolution simulations corresponds to the large-scale thermal tides and the augmentation of this range in high resolution models is associable with mesoscale topographic and surface property variations in the Gale Crater region. We show that the augmentation is due to the lateral redistribution of mass required for the surface pressure distribution over topographic relief to remain approximately hydrostatic as the near-surface air temperature varies through the diurnal cycle. The physical origin and nature of this adjustment flow is explored. We provide a means of predicting the daily surface pressure due to lateral hydrostatic adjustment for any location and further show that this range is slightly reduced by the inability of the atmosphere to completely achieve hydrostaticity and by the thermal effects of induced flows.

1. Introduction

Surface pressure on Mars provides a wide range of information about the dynamics of the atmosphere and climate. Uniquely for a point-measurement, the surface pressure provides column-integrated insight into the Martian atmosphere as it is, for the conditions existing there, solely proportional to the total atmospheric mass above any point on the surface and is completely insensitive to the vertical distribution of mass and temperature within the column (see Appendix A for a detailed discussion of the planetary atmospheric conditions for which this is true). The information contained in surface pressure measurements pertains to the variation of total atmospheric mass resulting from the CO_2 cycle (Hess et al., 1977) and the large-scale redistribution of mass corresponding to the mean meridional circulation (Haberle et al., 1982; Hourdin et al., 1993; Fenton and Richardson, 2001), thermal tides and Kelvin waves (Zurek, 1976; Wilson and Hamilton, 1996), transient waves (Barnes, 1980), and even very small-scale convective vortices (Schofield et al., 1997). However, a common feature of all sites sampled by surface meteorology stations prior to the Mars Science Laboratory (MSL) "Curiosity" rover (henceforth referred to simply as "Curiosity") has been relatively flat terrain and uniform surface properties on mesoscales. Note that length scales of atmospheric motion and forcing on Mars are

henceforth defined in this paper to be microscale for <5 km, mesoscale for 5–500 km, and synoptic scale for >500 km.

The observation of surface pressure in a region of complex mesoscale terrain on Mars became possible with the advent of Curiosity (Vasavada et al., 2012), which landed in Gale Crater, a region containing several kilometers of relief over scales of a few tens to hundreds of kilometers. Curiosity has been able to accurately measure pressure variations using the Rover Environmental Monitoring Station (REMS) (Gomez-Elvira et al., 2014; Harri et al., 2014), producing a dataset against which model predictions can be tested. Curiosity landed in late northern summer at planetocentric solar longitude, Ls ∼ 150° and has now operated for over three martian years. An aspect of the observations that is immediately striking is the large diurnal range of surface pressure (hereafter DRSP). Note that we use the DRSP to designate the true minimum-to-maximum daily range of pressure and not the amplitude of the surface pressure oscillation about the daily mean. In the sols following landing, the observed DRSP was measured to be about 11% of the daily average value, as shown in Fig. 1a (Harri et al., 2014), with a peak near 08:00 hour Local Time (LT) and a minimum near 17:00LT. (Note that we use 'hour' to refer to 1/24th of a Martian solar day, where the Martian solar day is longer than its terrestrial counterpart at 88,775s in mean duration. The Martian solar day is sometimes referred to as a "sol," or capitalized as "Sol" when
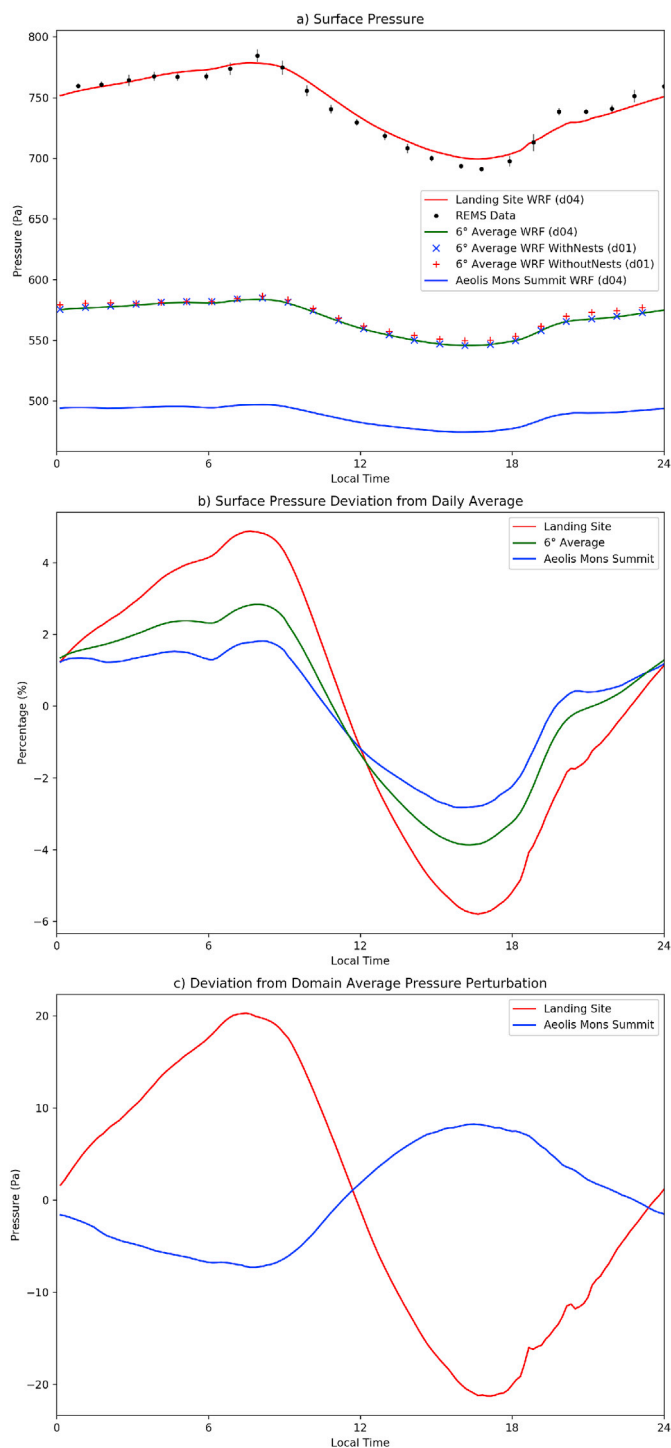
---

* Corresponding author.

  E-mail address: mir@aeolisresearch.com (M.I. Richardson).

a) Surface Pressure

b) Surface Pressure Deviation from Daily Average

c) Deviation from Domain Average Pressure Perturbation

(caption on next column)

Fig. 1. The variation of surface pressure observed at the Curiosity landing site and simulated for the same location by MarsWRF as a function of local true solar time. **(a)** Pressure predicted in mesoscale simulation WithNests d04 domain (red line) and observed (black dots with vertical error bars) at the Curiosity landing site. The error bars represent the variance in pressure of the observations that have been binned by hour over 20 Sols (from mission Sol 10–30). The rough agreement between the observed and predicted pressure suggests that the model captures the observed diurnal cycle adequately for the purposes of this study. This panel also shows the average of the surface pressure over a $6° × 6°$ box centered on the landing site. The area average is shown for the d04 domain from WithNests (green line), for the d01 domain from WithNests (blue crosses), and the d01 domain from WithoutNests (red pluses). Finally, this panel also shows the pressure variation over the summit of Aeolis Mons (Mount Sharp) for domain d04 from WithNests (blue line). **(b)** The diurnal cycle of pressure perturbation in WithNests d04 as a percentage of the diurnal mean at the Curiosity landing site (red line), for the domain average (green line) and the summit of Aeolis Mons (blue line). **(c)** The deviation of pressure at the Curiosity landing site (red line) and at the summit of Aeolis Mons (blue line) from the instantaneous domain average pressure in WithNests d04. (For interpretation of the references to colour in this figure legend, the reader is referred to the Web version of this article.)

Martinez et al., 2017).

Despite its unprecedented amplitude, the strength of the DRSP within Gale Crater is captured in mesoscale model simulations. Numerical modeling of flows over complex terrain with Mars mesoscale numerical models began almost two decades ago, with spacecraft landing site assessment a significant practical focus (Rafkin et al., 2001; Toigo and Richardson, 2002, 2003; Tyler et al., 2002; Golombek et al., 2003). The models have also been used to assess the impact of flow over complex terrain on ground and air temperatures (Spiga et al., 2011). The large DRSP that was ultimately observed by Curiosity was first noted in a multi-model study of the Curiosity landing site prior to the mission (this work was done by a combination of members of the REMS science team and the MSL council of atmospheres, but a manuscript describing the work by Haberle and co-authors 2012, and submitted to the Mars Journal, remains unpublished; henceforth we refer to this multi-party study as the "multi-model study"). These numerical simulations showed that the diurnal range of surface pressure within the trough of Gale Crater is substantially larger than on the surrounding plains (about 11% in the trough *vs.* 6% on the plains at the landing season – note that we use "trough" to refer to the low elevation interior of Gale Crater between the crater rim and Aeolis Mons). These and later simulations have been separately detailed for the National Center for Atmospheric Research (NCAR) Weather Research and Forecasting model used in this study (MarsWRF, see Appendix B and Fig. 1a) (Richardson et al., 2013), the NCAR Mesoscale Model version 5 (MMM5) (Tyler and Barnes, 2013, 2015), and the Mars Regional Atmospheric Modeling System (MRAMS) (Rafkin et al., 2016). Fig. 2a shows maps of the percentage DRSP, calculated as $100 ×$ the diurnal range in surface pressure divided by the daily mean surface pressure, and referred to hereafter as PDRSP. The PDRSP maps are very similar in all three models, as can be seen by comparing Fig. 2a with Fig. 8a of Tyler and Barnes (2013) and Fig. 16 of Rafkin et al., (2016).

The multi-model study provided comparison of mesoscale models with lower resolution global general circulation models (GCMs, typically with a few degrees horizontal grid spacing). It was found that a model resolution of better than about 5 km is necessary to properly simulate the large DRSP at the landing site. At 2–5° grid spacing, GCMs generally yield DRSP for the landing site that is nearer to that of the value predicted for the plains (about 6%). Subsequently, this was also shown by Tyler and Barnes (2013, 2015), Richardson et al., (2013) and Rafkin et al., (2016). Richardson et al., (2013) and Rafkin et al., (2016) further point out that the geographical variation of the DRSP is a strong function of topography within the Gale Crater region (see also Section 2). In aggregate, these findings suggest the augmentation of DRSP – *i.e.,* the increase produced by mesoscale models compared to coarser resolution models – is
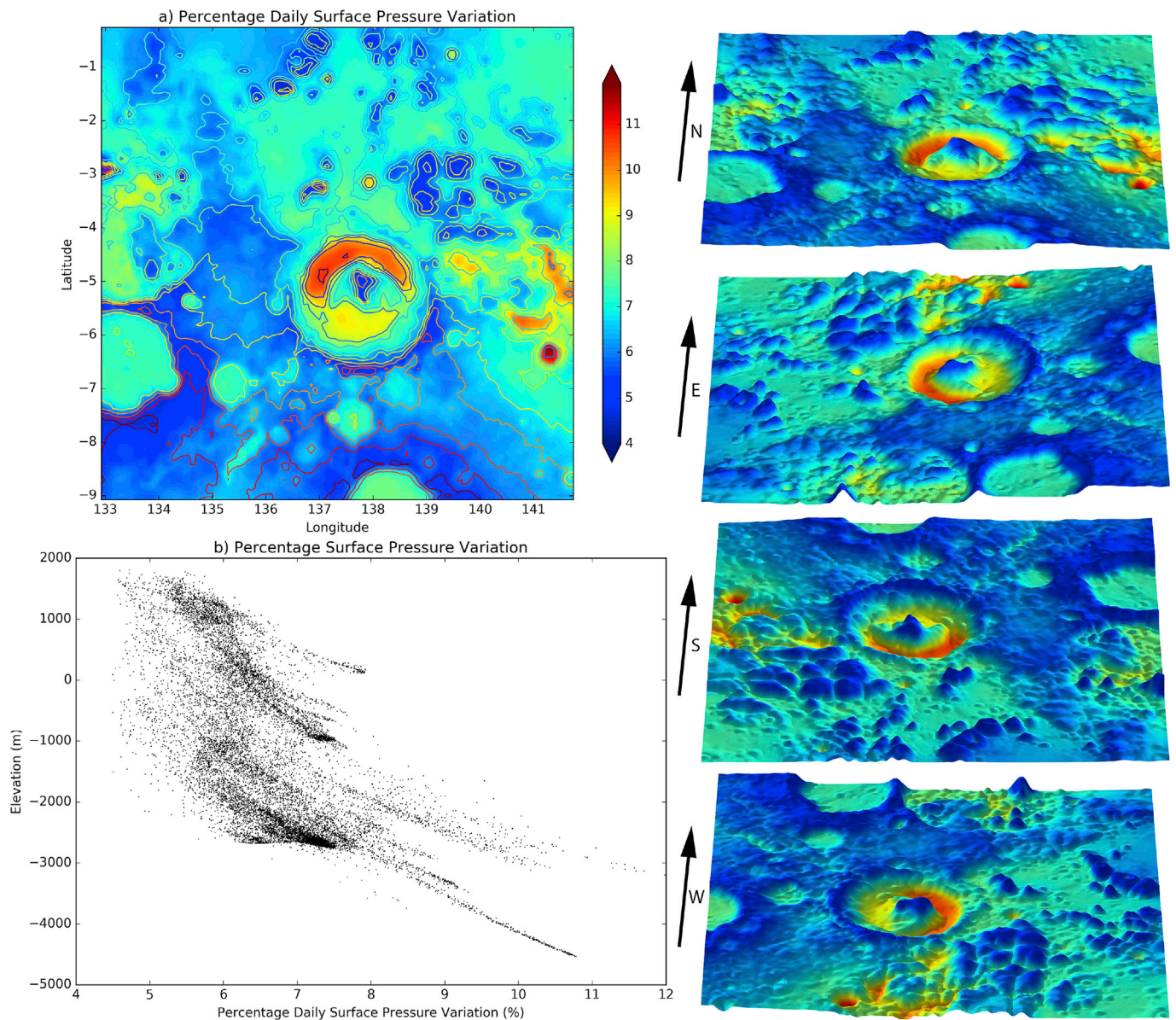
referring to the Martian solar day number since the Curiosity landing during Sol 0). This daily pressure range has proven repeatable when these seasonal dates were resampled in subsequent years and is large throughout the annual cycle, varying from about 7% to over 13% (Martinez et al., 2017). While a significant diurnal variation of surface pressure is expected due to the large amplitude of the thermally driven diurnal tide (Guzewich et al., 2016), the observed range is unusually large compared to all previous lander measurements. As an example, it is about twice the daily variation observed by Mars Pathfinder, which operated for a limited period around Ls = 150° (Harri et al., 2014,

Fig. 2. The percentage DRSP in WithNests d04. **(a)** A map of percentage DRSP overlain with contours showing elevation of topography. The same data are shown draped on the topography and in projections looking to the north, east, south, and west (as indicated) in the right hand column. **(b)** The DRSP plotted against elevation for each point in d04.

associated primarily with direct, periodic thermal forcing of the atmosphere over topography with large mesoscale variation. But the question remains: by what physical mechanism does this augmentation occur? This question is the main focus of this paper.

Section 2 discusses the nomenclature and dynamical phenomena involved in this study, while Section 3 discusses prior work and describes how different uses of nomenclature has previously caused some confusion. In Section 4, we introduce the REMS surface pressure data from late northern summer, which provides the starting point for the present study. The late summer period was when the very large DRSP was first identified just after landing (Harri et al., 2014), although it has subsequently been found to be robust throughout the annual cycle (Martinez et al., 2017). We use the REMS observations to calibrate numerical model simulations (see Appendix B) and use the model to provide a proxy for reality in order to characterize the diurnal variation of the surface pressure field across the whole Gale Crater region and to provide a clean illustration of what is meant by DRSP augmentation. In Section 5 we test the proximity of the lateral surface pressure distribution across the Gale

Crater region to a state of hydrostaticity, examine how the modeled and hydrostatic surface pressure distributions change with local time, and consider the influences upon this hydrostatic state. In Section 6, we propose that the mass redistribution responsible for the DRSP augmentation is driven by a lateral flow needed to maintain proximity to a hydrostatic pressure distribution throughout the daily thermal cycle, and explore the physics and consequences of such a flow. Finally, in Section 7 we provide a brief summary.

2. Nomenclature and the dynamics of relevant atmospheric flows

A variety of circulation processes operate within the atmosphere and the terms used in atmospheric dynamics to label these processes can range from being purely descriptive in nature (in which case the term does not specify the controlling physics) to being very specifically genetic (in which case the name can be linked to a very specific physical mechanism). It is essential that we begin our discussion with a clear definition of terms, since it then becomes possible to understand how the

labels used for flows relate to specific mechanisms, how concepts used in one paper relate to those in another, and how terms used in this and our subsequent papers can be related to standard reference definitions and equations (*e.g.,* Pielke (2002) and Mahrt (1982)). Unfortunately, many of the terms we need to use in this paper have been applied variously in the literature both descriptively and genetically, as have a wide range of synonym terms. The most problematic terms for the purposes of understanding the DRSP at Gale Crater are the terms "tide" and "slope flow." We thus pause here to carefully define how we will use these terms in this study.

2.1. Tides

The term 'tide' is taken from an old English word meaning an interval of time and has morphed over the ages to become associated specifically with the intervals of time demarcated by the periodic rising and falling of the sea (see the Oxford English Dictionary). The term's antiquity means that it is descriptive in this sense, antedating understanding of how the seas rise and fall under the gravitational influence of the Moon. The current usage of the term "thermal tides" in atmospheric dynamics draws on the analogy between differential gravitational and differential thermal forcing of geophysical fluids. If used most generally, "thermal tide" can thus be applied to reference any variation in the atmosphere caused by the diurnal cycle of heating, albeit at the cost of losing any deeper connection to physical mechanism. Indeed, it is sometimes very useful to do this, such as when wanting to quantify the thermal tide by fitting harmonics to landed surface station pressure measurements (*e.g.,* most recently and for the Curiosity site see Guzewich et al., 2016). In these cases, all variations with periods that are harmonic with the diurnal cycle are described as tides. However, "tide" as used in classical tidal theory, linear tidal models, and in the interpretation of global tides in atmospheric models is more genetically specific (*e.g.,* Wilson and Hamilton, 1996, and the Appendix of Wilson and Richardson, 2000). "Thermal tide" in this context refers to global-scale inertia-gravity waves and Kelvin waves that are excited by the diurnal variation of atmospheric heating and interaction with large-scale topography; that propagate spatially under the influence of the varying atmospheric static stability and the varying Coriolis parameter; and that are modified by interactions with other circulation components.

A dynamically meaningful or genetic definition of atmospheric thermal tides therefore includes both the spectrum of migrating and non-migrating modes (see, *e.g.,* Wilson and Hamilton, 1996). The vast majority of the power in these genetically defined thermal tides is at long (synoptic) wavelengths (Wilson and Hamilton, 1996). Since all prior cases of Mars lander pressure data analysis have been conducted at sites where (on mesoscales) the surfaces have been generally flat and in areas of relatively uniform thermo-physical properties, there has been little need to worry about confusing daily harmonics of surface pressure resulting from the synoptic-scale genetic thermal tide with unrelated but diurnally forced mass redistribution by mesoscale circulations. Thus, the distinction between the tide as defined as any diurnal variation and the more specific (genetic) definition as large-scale wave modes has previously been moot. The Curiosity site is the first location for which the distinction is not moot, hence in this paper we specifically use the genetic definition of thermal tides.

2.2. Slope flows

Using purely descriptive terminology, any flow associated with varied terrain can be labeled as 'slope flow'. However, there are several distinct mechanisms of slope-related flow acceleration that exist and these are best separately labeled for physical clarity. Two major subdivisions of slope flows are (1) the acceleration of a larger-scale lateral background flow as it moves over an obstacle and (2) the direct thermal induction of a flow over a slope without the need for an imposed wind.

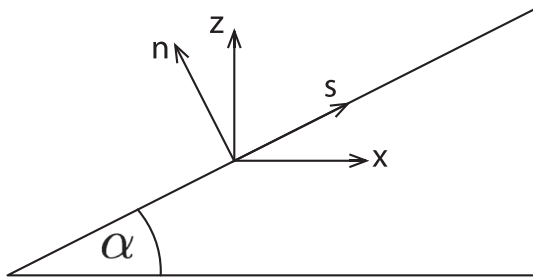#### 2.2.1. Acceleration of existing flow over obstacle

Flows associated with the acceleration of background winds are often referred to in the literature as down-slope windstorms (*e.g.,* Baines, 1998; Durran, 2003; Pielke, 2002). They occur with the transition from wave-like to non-wavelike flow over an obstacle, and more generally with flow transitions from super-critical to sub-critical. Criticality is determined based on the Froude number (Fr), which is related to the (square root of the) background flow kinetic energy (KE) divided by the potential energy (PE) gained by flow over the obstacle. In this sense, the Froude number can be thought of as the inverse of a non-dimensional obstacle height. The Froude number is also a measure of the flow speed relative to gravity wave speeds and thus provides a gauge of whether the mass and flow fields can adjust to the presence of the obstacle. At high Fr, the flow tends to 'ride over' the obstacle, transitioning some KE into PE and back to KE. On the other hand, at low Fr, the flow 'notices' the obstacle and both flows around it and speeds up over it. When there is a transition from low to high Fr over the obstacle, the downstream and upstream flows become asymmetric, with a distinct acceleration of the downstream flow. Downslope windstorms at Gale Crater are described in more detail by Rafkin et al., (2016) and are readily identifiable in mesoscale model output. They are not a major focus in this paper as we will show that much simpler, thermally-induced topographic flows can explain essentially all of the DRSP augmentation at the Curiosity landing site.

2.2.2. Thermally induced topographic flows

We discuss three genetically distinct types of thermally induced topographic flows in this paper: the buoyancy slope flow, the slope-modified sea breeze flow, and the lateral hydrostatic adjustment flow.

2.2.2.1. Buoyancy slope flow.

Buoyantly unstable flow along a slope is the primary kind of thermo-topographic flow described in the terrestrial literature; however, several different labels have been used. "Buoyancy slope flow" is used without association with a specific flow direction, while "gravity flow," "drainage flow," and "katabatic flow" specifically refer to downslope-directed buoyancy slope flows, and "anabatic flow" to upslope buoyancy slope flows. Note that although 'anabatic' and 'katabatic' are sometimes used to mean any upward or downward flow (their Greek origins suggest just this, since, *e.g.,* 'anabatic' is derived from 'anabainein' meaning to move uphill, or in the case of Xenaphon's Anabasis, to march an army "up country" – potentially confusingly, since Xenaphon actually spends most of his narrative marching the army back "down country"), their usage in mesoscale meteorology has been almost exclusively genetic in application to buoyancy slope flows (Durran, 2003). Regardless of label, the buoyancy flow is defined as the along-slope surface level flow acceleration resulting solely from the buoyancy of the near-surface air relative to that of the 'environmental air' on the same level but at a distance from the sloping terrain surface (Mahrt, 1982; Ye et al., 1987, 1990; Pielke, 2002; Haiden, 2003).

As described by, *e.g.,* Mahrt (1982) and Haiden (2003) (and in more detail in Part 2 of this sequence of papers), the equations describing the buoyancy slope flow are derived from a simplified set of the primitive equations after rotation of the horizontal and vertical coordinates into the along-slope and slope-normal directions, respectively (see Fig. 3 for the definitions of the along-slope, horizontal, slope-normal, and true vertical directions). The driving buoyancy force corresponds to the first term on the right-hand side (RHS) of equation (9) from Mahrt (1982); specifically g $(\theta/\theta_0)\sin\alpha$, where g is the gravitational acceleration, θ is the perturbation potential temperature near to the surface, θ_0 is the basic state potential temperature away from the buoyancy flow, and α is the surface slope. The term is very similar to that considered in thermal convection, and buoyancy slope flows can be considered in some sense as a form of "sloping surface" thermal convection. This has important implications for buoyancy slope flows as it means that the sign of the
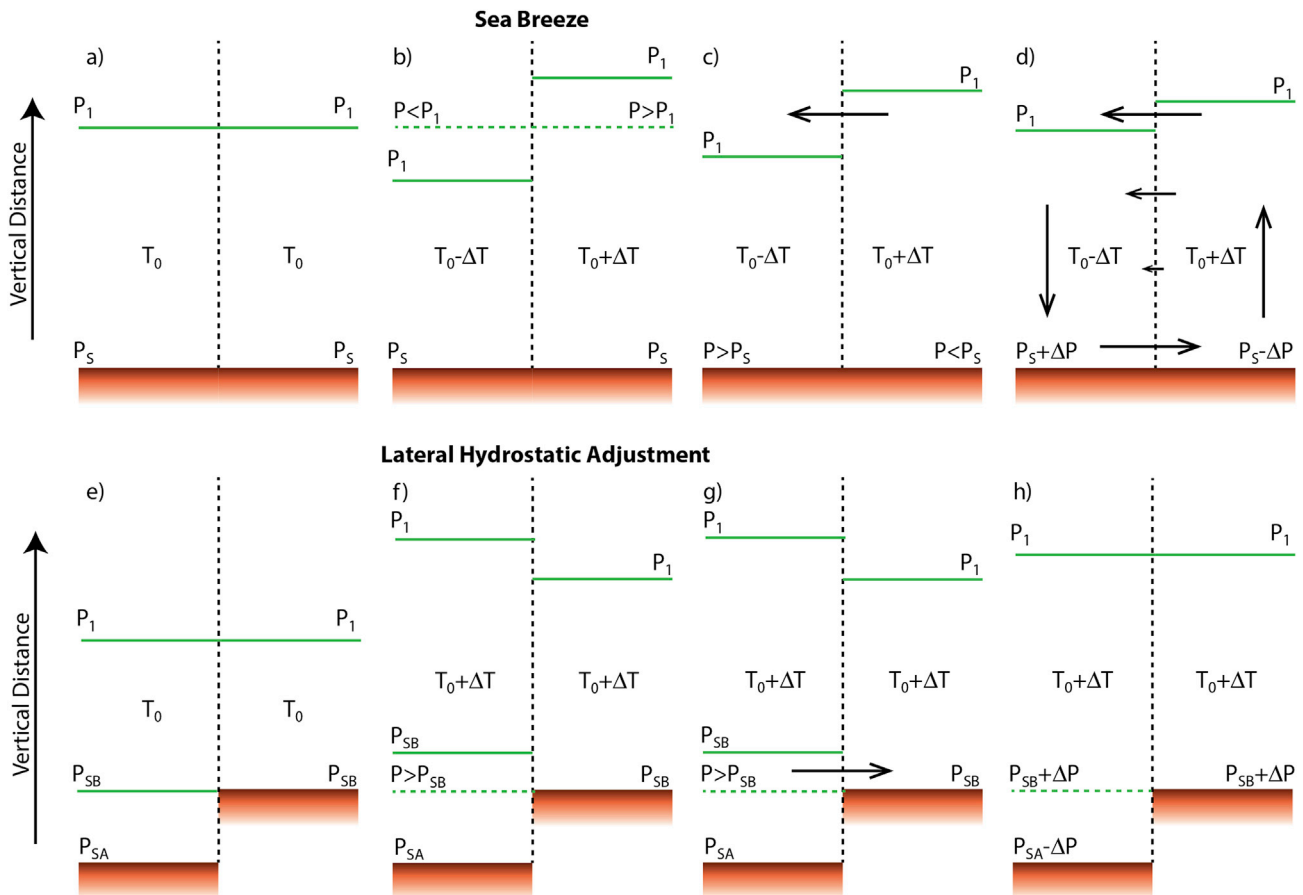
Fig. 3. Definitions of the vertical and horizontal directions relative to the slope and relative to the gravity vector. The true vertical direction is defined as the negative "along the gravity vector" direction, z, with the true horizontal direction being normal to it, x. For a sloping surface at angle, α, the along slope direction is defined as s, with the slope normal direction being n.

surface-atmosphere (sensible plus radiative) heat flux above the sloping terrain determines the direction of buoyancy slope flows (Ye et al., 1987): if the surface heat flux is positive (*i.e.,* if there is net heat transfer from the surface to the air), the flow acceleration is upslope, and vice versa. This is true irrespective of whether the total surface-atmosphere system is cooling, heating, or at a fixed steady state temperature.

Most significantly for the purposes of this paper, the buoyancy flow governing equations do not modify the along-slope surface pressure gradient (Mahrt, 1982; Pielke, 2002; Haiden, 2003). This non-mass redistributive requirement emerges naturally as a consequence of the definition of the buoyancy slope flow as resulting from the imposition of a thermal perturbation distribution (*i.e.,* where 'perturbation' means there is zero spatial-average) upon a non-changing hydrostatic base state.

With this definition, the near-surface flow is always balanced by an upper level return flow with no net lateral transport of mass. This non-mass transportive nature of buoyancy flows is revisited in much greater detail in Part 2 of this series of papers.

2.2.2.2. Slope-modified sea breeze flow. The slope-modified "sea breeze" circulation relates the along-slope flow acceleration to the along-slope thermal gradient and corresponds to the second term on the RHS of Eqn. (9) from Mahrt (1982). In the limit of a flat surface, this flow corresponds to lateral differences in diabatic heating of the air, such as occurs over lateral variations in ground temperature due to variations in albedo, thermal inertia or emissivity. Following the most common theory of sea breeze spin-up (Pielke, 2002; Miller et al., 2003), the relationship between the evolution of the thermal structure, pressure structure, and winds in the sea breeze flow is illustrated in Fig. 4a–d, which shows a lateral domain divided into two columns. With the temperature and pressures initially in equilibrium, there is no flow. As a perturbation temperature gradient is introduced between the two columns comprising the domain (Fig. 4b), the warmer right hand column expands relative to the cooling left hand column, creating a lateral pressure gradient at altitude. The figure shows the height of only one representative pressure level (P_1) at altitude, but the elevation separation across the thermal discontinuity grows continuously with height. Fig. 4b is illustrative in that it represents an idealized non-equilibrium state after the vertical pressure distribution has adjusted to the imposed temperature change but before lateral mass flows have been initiated due to the resulting lateral pressure gradients at height. In response to the pressure gradient at altitude, an upper level flow is induced from the warm to the cool column (Fig. 4c). This flow is mass redistributive and moves net mass from the warm to the cool column, and as a result, a surface pressure

Fig. 4. Schematic illustrating the relationship between the evolution of the thermal structure, pressure structure, and winds in the **(a–d)** sea breeze and **(e–h)** hydrostatic adjustment flows. See text in Section 2.2.2.2 for more details.

gradient develops in the direction opposite to that of the pressure gradient at altitude. The development of a surface pressure gradient causes the acceleration of a low level flow from the cool to the warm column (Fig. 4d). To complete the circuit and in order to maintain vertical hydrostatic balance in each column, descending air is required in the cool column and ascending air is required in the warm column.

The steady-state lateral surface pressure gradient is determined by the lateral temperature contrast, and once the surface pressure distribution has come into this balanced steady-state the net lateral transport of mass ceases. This state corresponds to a mass balance between the upper and lower level flows. However, even after the net lateral mass transport has ceased, the circulation will continue to accelerate until either checked by friction or until advection laterally homogenizes the thermal contrast; *i.e.,* until all the baroclinically available potential energy is used. It should also be noted that the surface level winds and the mass transport (while it persists) are not related to each other in a simple way: the net mass flow is always from the warming to the cooling column (and tends to zero as the lateral surface pressure distribution adjusts to a new, fixed lateral temperature distribution), while the surface level wind acceleration is from the cool to the warm column (and continues to accelerate irrespective of whether the surface pressure gradient is in balance with the thermal contrast). In the presence of a slope, the relationship between the thermal contrast and the lateral pressure gradient is quantitatively modified, but the qualitative dynamics described here remain unchanged (Mahrt, 1982).

2.2.2.3. Lateral hydrostatic adjustment flow. Terrestrial theory defines the above two types of slope flows relative to a fixed background hydrostatic state - *i.e.,* by introducing thermal perturbations that do not change the domain-average temperature (or more accurately, do not introduce a domain-average net heating). However, almost everywhere on Mars there is a large diurnal variation of the background thermal state. This increased importance of the daily change of mean near surface air temperature on Mars, where it is typically 50–80K, relative to the Earth, where it is more typically 5–20K, is important for our introduction of a third thermo-topographic flow in this paper. Termed the lateral hydrostatic adjustment flow, it operates alongside the slope buoyancy and sea breeze flows and is crucial to explaining the high DRSP observed in Gale Crater.

Like the sea breeze flow, but unlike the buoyancy slope flow, the hydrostatic adjustment flow is able to modify the surface pressure distribution along a slope. For the hydrostatic adjustment flow a lateral difference in elevation of the two columns is required. We draw this in Fig. 4e–h as a step function but this is just for diagrammatic simplicity (a slope of any reasonable shape is entirely equivalent). The initially isothermal atmosphere has the same pressure structure in the deeper (A) and shallower (B) columns, with the surface pressure, P_{SA}, being larger that P_{SB} solely due to the difference in elevation of the two columns. Within column A, the absolute elevation of the P_{SB} pressure level is that of the surface in column B. When a uniform temperature perturbation is added to the isothermal atmosphere (Fig. 4f), both columns expand, but this would cause the elevation of the P_{SB} level to rise above the elevation of the surface in column B. However, as no mass has been added to column B (and if we assume that the heat is added slowly), its surface pressure cannot increase. As with Fig. 4b for the sea breeze flow, Fig. 4f is illustrative as it corresponds to an idealized state in which the vertical pressure distribution has fully adjusted to the thermal perturbation, but in which no lateral motions have yet been initiated in response to the lateral pressure gradients that develop between the columns. Indeed, the pressure gradient that develops between column A and column B necessarily causes a net transport of mass from column A to column B (Fig. 4g). The pressure gradient is eliminated (Fig. 4h) when sufficient mass is moved between the columns such that the $P_{SB}+\Delta P$ layer that defines the surface pressure in column B is at the same absolute altitude in column A.

The flow of mass that is needed to restore the hydrostatic balance along the lateral surface elevation contrast as the uniform air temperature is changed is the hydrostatic adjustment flow. Similar to the sea-breeze flow, net lateral transport only ceases when the surface pressures have adjusted to the new thermal state, although unlike the sea breeze flow, the hydrostatic adjustment flow has no non-mass transportive component that continues after adjustment. This is because, while there remains available potential energy in the post-adjustment sea breeze state due to the lateral thermal contrast (Fig. 4d), there is none in the post-adjustment hydrostatic flow state (Fig. 4h).

3. Prior discussion of the origin of the large DRSP within Gale Crater

At the Curiosity landing site, the general temporal structure of the daily pressure cycle, roughly half of the diurnal amplitude of this cycle, and the dependence of the daily pressure cycle on factors such as global atmospheric dust loading, are clearly attributable to the genetically-defined thermal tides (Harri et al., 2014; Guzewich et al., 2016). This thermo-tidal contribution to the DRSP is already large relative to other locations on the planet due to the landing site's tropical latitude and due to the constructive interference of the westward migrating diurnal tide and the diurnal Kelvin wave over its general longitude (Leovy and Zurek, 1979; Wilson and Hamilton, 1996; Guzewich et al., 2016). However, notwithstanding this large tidal DRSP, even models that provide a full simulation of the genetic thermal tides but that do not resolve topography on scales of <5 km fail to capture up to 50% of the DRSP as observed by REMS. Thus the augmentation in the DRSP defined earlier may be equivalently defined as the augmentation relative to the purely thermo-tidal variation of surface pressure. This augmentation must be associated with how flows develop over the mesoscale topography under the influence of daily thermal forcing. Richardson et al., (2013), Tyler and Barnes (2013; 2015) and Rafkin et al., (2016) all agree on this point, which was already obvious from the multi-model studies. However, there has previously been less agreement as to its cause.

Tyler and Barnes (2013; 2015) provide very detailed descriptions of how the thermal structure in the Gale Crater region changes in response to the diurnal thermal forcing over terrain. They suggest that most of the DRSP augmentation is due to adiabatic modification of the thermal structure by the flows within the crater. In this conception, the DRSP depends upon the thermal structure, which in turn is principally controlled by flows associated with the mesoscale topography. Yet it is unclear from their description what is driving these flows (*i.e.,* what the important force balances are) or how they link to genetic definitions of flows found in the terrestrial literature, and no quantitative theory is provided for estimating the size of the augmentation. They examine the mass flowing in and out of the crater by integrating the hydrostatic equation downwards from a level in the free atmosphere using a variety of thermal structures, but while this has diagnostic interest such calculations have little prognostic capability and have thus yielded no conceptual insight. By contrast, the approach of Richardson et al., (2013), Rafkin et al., (2016), and this paper focuses on extracting a causal relationship between the atmospheric forcing and surface pressure by considering the along-slope momentum equation.

Tyler and Barnes (2013, 2015) label the flow responsible for the DRSP augmentation as the "crater flow" or "crater circulation." While superficially appealing, there are two major problems with using this terminology. The first is that it provides no genetic information on how the flow functions. Since the problem, as posed by the multi-model study, was to explain how the circulation over Gale Crater causes the daily range of surface pressure in the crater trough to be augmented relative to tidal expectations, it is clear that "crater circulation" does not provide a meaningful answer: it is simply a relabeling of the problem. The absence of a specific, genetic mechanism for the "crater circulation" also means that it provides no hypothesis that may then be tested scientifically. Possibly Tyler and Barnes (2013, 2015) envisioned some combination of

buoyancy slope and slope-modified sea breeze circulations, but this is never specified. The second problem is that the usage of 'crater' within the label implies that there is something special about craters, as opposed to other topographic features, that is important in driving the flow that augments the DRSP. Yet even at the Curiosity landing site, Aeolis Mons (Mt. Sharp) appears to be at least as important for the mesoscale meteorology as the crater topography (Rafkin et al., 2016; Newman et al., 2017). The question of whether there is anything special about craters as regards the primary mechanism responsible for the DRSP augmentation, and whether the lessons learned from Gale are applicable to other sites and types of topography, is revisited in Part 3 of this sequence of papers. Finally, Tyler and Barnes (2015) use an isolated mesoscale model (*i.e.,* without any synoptic scale forcing) to demonstrate that the thermal tide is not responsible for the DRSP augmentation. One could be forgiven for thinking that this was a foregone conclusion since the problem posed by the mutli-model study was to explain why the DRSP is larger than produced purely by the genetic thermal tide, and thus clearly the tide could not - by the very definition of the problem - be the explanation.

Richardson et al., (2013) and Rafkin et al. (2016) both point out that the surface pressure distribution throughout the diurnal cycle and across the varied terrain of the Gale Crater region remains close to a state of hydrostatic balance. This proximity is maintained even though there is a very significant diurnal cycle of ground and near surface air temperatures. The diurnal range of ground and near-surface air temperatures are much larger than the horizontal variation of either variable at a given local time (see Section 5.3). Since the large changes in air temperature correspond to large changes in the scale height, the spatial pattern of the surface pressure over the complex terrain is required to change significantly in order to retain or approximate hydrostatic balance. The existence and nature of this rebalancing is the topic of much of this paper. In Richardson et al., (2013) and here, this redistributive flow is referred to as the hydrostatic adjustment flow (note that this is not directly related to the *vertical* hydrostatic adjustment problem (Bannon, 1995)). In Rafkin et al., (2016), they state that the redistribution needed to accomplish this hydrostatic rebalancing is driven by "tides", however it is clear from the paper that they are using the descriptive rather than the genetic definition of thermal tides, and they use the term only to refer to the daily cycle of heating/cooling. Despite the terminological confusion, the remainder of their description in the paper also makes it clear that they are describing a strongly convergent/divergent (*i.e.,* surface pressure redistributive) circulation that drives the atmosphere towards hydrostatic balance along varied terrain, as in Richardson et al., (2013) and this paper.

4. Variation of surface pressure across the Gale Crater region

In this section, we examine the spatial and temporal variation of surface pressure across the Gale Crater region using MarsWRF model output that has been calibrated against the REMS surface pressure observations. We use model output as a proxy for reality rather than the observations directly, because the REMS observations do not sample a sufficient range of elevations over the Gale Crater region. Curiosity has climbed over 335 m in elevation at the time of writing, but comparison with Fig. 2b shows that this is still a very small fraction of the elevation range present in the Gale Crater region. It is possible that the sampling of the elevation range by Curiosity may be sufficient for direct analysis of the pressure data at some distant point in the future, depending on how far up Aeolis Mons the rover eventually ascends. Instead, in this paper, two MarsWRF simulations are used: (i) "WithOutNests" – a standard global simulation at 2° horizontal resolution, and (ii) "WithNests" – another global simulation at 2° resolution but with three increasingly high resolution domains recursively 'nested' within it to ultimately achieve a resolution of about 4.4 km in the innermost nest (domain 4 or d04). The domain resolutions are summarized in Table 1 and more details on the simulations and the MarsWRF modeling system as used in this study are provided in Appendix B. The "WithOutNests" simulation is very

similar to that previously described for MarsWRF by Guzewich et al., (2016), while the "WithNests" is very similar to that used by Newman et al., (2017) but uses two fewer levels of nesting. The choice of d04 as the final nest for this work stems from examining the daily variation of pressure at the simulated Curiosity landing site, which increased as the MarsWRF resolution was increased to that of the d04 domain but was unchanged with the addition of higher-resolution d05 and d06 domains (with resolutions of about 1.5 km and 500 m, respectively).

4.1. The local time variation of surface pressure

The diurnal cycle of pressure predicted by the WithNests simulation for late northern summer at the Curiosity site is shown as the upper curve in Fig. 1a (red line) along with early mission REMS pressure data (Sols 10–30, shown in black) (Harri et al., 2014). The model output comes from the d04 grid point closest to the landing site (see Fig. 5g, which shows the landing site location within d04; Fig. 5 is discussed in greater detail later in the paper). The elevation difference between the actual landing site and model grid point used is only 10 m. A potential complicating factor in the use of REMS pressure measurements is that they were collected from a moving platform, with all prior surface pressure datasets having been taken from stationary platforms. The multiyear REMS dataset shows a general decrease in daily-average pressure during the mission (*e.g.,* Martinez et al., 2017), which is due to the fact that Curiosity has generally been driving uphill from its landing site (*e.g.,* by late June 2018, the rover elevation was about 335 m higher than at landing). We selected only a very short period of data to show in Fig. 1a during which the change in elevation of the rover was not significant. From the comparison, we conclude that the high-resolution version of MarsWRF does a good job matching the observed pressure cycle, and in particular the observed DRSP.

The middle three curves (red plus signs, blue crosses, and green line) in Fig. 1a show output from respectively (i) the WithOutNests global run, (ii) WithNests domain 1 (d01; the global domain), and (iii) WithNests d04, in each case averaged over a $6° \times 6°$ box centered on the Curiosity landing site and covering the same geographical area. This box size is taken as being characteristic of most published GCM resolutions, which have typically varied from about $5° \times 5°$ to $7.5° \times 9°$, and results in the average being over a 3×3 grid in the WithNests and WithOutNests global domains and over an 81×81 grid in WithNests d04. All three sets of model output lay closely on top of each another, emphasizing the consistency between them.
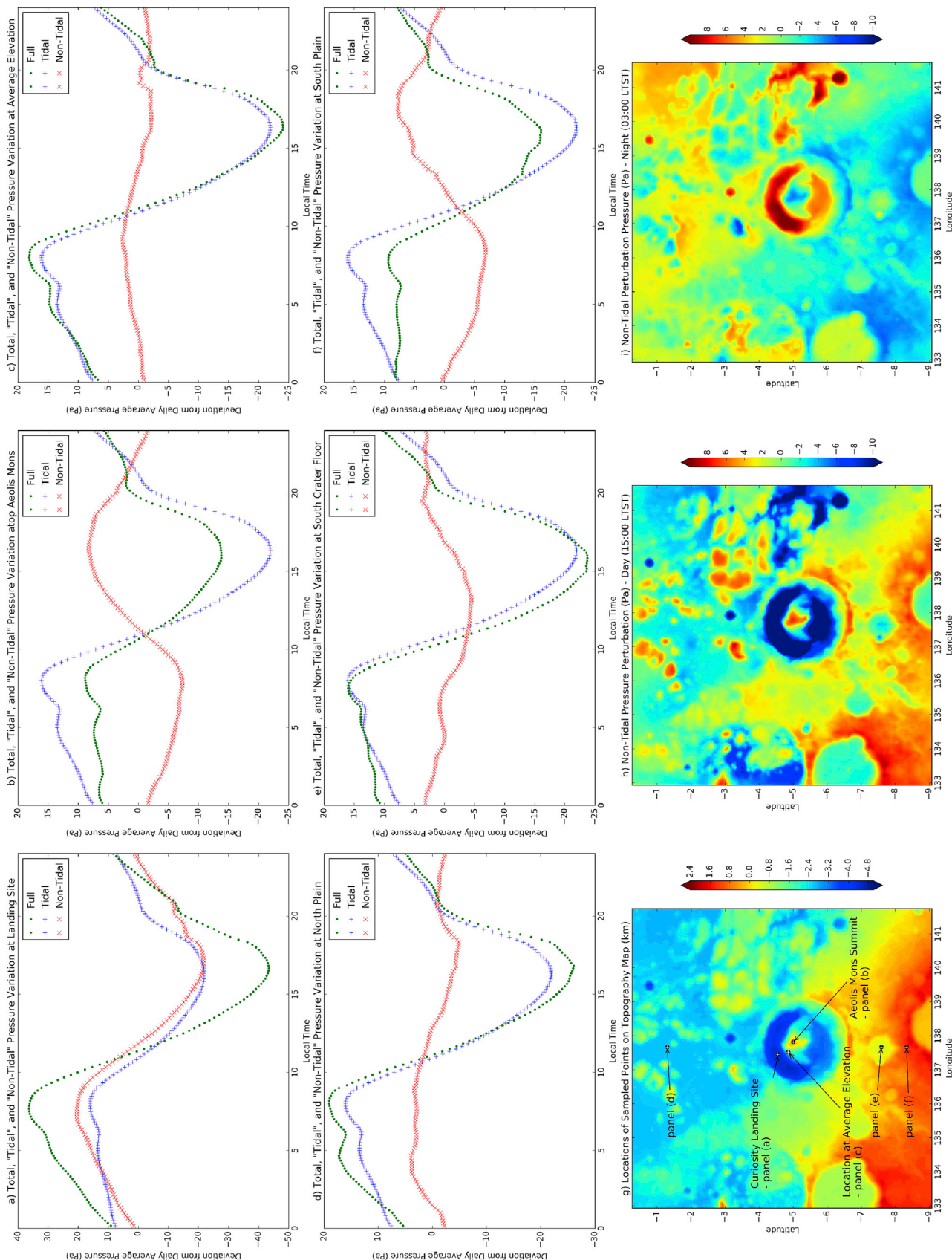
The purpose of comparing the pressures in these $6° \times 6°$ boxes is twofold. It confirms that the same model can simultaneously generate a good match to observations when topography is resolved while also agreeing with low resolution GCM expectations when realistic topographic variation is not resolved. More importantly for the purposes of this paper, it illustrates the finding from the multi-model study that the processes leading to the amplification of the diurnal pressure at the Curiosity landing site *must* be due to purely local redistributions of mass on mesoscales unresolved by a typical GCM and which are consequently "averaged out" over an area equivalent to an individual GCM grid cell.

The lowest curve (blue line) in Fig. 1a corresponds to the topographically highest location within d04, which sits atop Aeolis Mons and is also indicated in Fig. 5g. The decrease in mean pressure is due simply to

Table 1

MarsWRF simulations and domains used in this study. The simulation names are listed in the first column. The domain resolutions are given in each row. Only global domain (d01) and the third nest (d04) are used in this study for the WithNests simulation. Only the global domain (d01) was run and is shown for the WithOutNests simulation (see Appendix A for more details).

	d01	d04
WithNests	2°/120 km	0.074°/4.4 km
WithOutNests	2°/120 km	n/a

Fig. 5. (A–f) The daily variation of tidal, non-tidal and total surface pressure at six locations within the Gale Crater complex and on surrounding terrain. Within Gale, **(a)** the Curiosity site, **(b)** the peak of Aeolis Mons, and **(c)** a location on the flank of Aeolis with the average elevation are shown. **(d–f)** Points north and south of Gale Crater at differing elevation are also shown. **(g)** The locations of the sampled points are indicated on a topographic map of the domain. Maps of the non-tidal component of the surface pressure variation are shown for **(h)** 15:00 and **(i)** 03:00 local time.

the increase in elevation.

4.2. The percentage diurnal range of surface pressure

The elevation differences between the three regions shown in Fig. 1a make it difficult to assess the relative sizes of the daily pressure ranges because the mean surface pressure differs significantly between them. More readily intercomparable is the PDRSP, which shows the deviation from the diurnal mean as a percentage of the diurnal mean, following Tyler and Barnes (2013) (Fig. 1b). Red, green and blue again refer to the landing site, $6° \times 6°$ average, and Aeolis Mons summit, respectively. From Fig. 1b it is clear that there is a dramatic decrease in PDRSP between the crater floor (where it is more than 11%) and the top of Aeolis Mons (where it is less than 4%). The similarity of the shape of the diurnal variation of pressure at the various points within the Gale Crater system is because this shape is largely determined by the synoptic scale thermal tides (e.g., Guzewich et al., 2016).

A full mapping of the relationship between PDRSP and topography in the Gale Crater region is shown in Fig. 2a. The apparent strong correlation suggests that PDRSP may be tightly controlled by elevation. We test this by plotting the PDSRP at each grid point as a function of elevation in Fig. 2b. As all points do not fall along a single line, it is clear that the PDRSP cannot be a simple function of elevation alone. Rather, the model output shows multiple bands along paths that arc from low PDRSP at higher elevation to high PDRSP at lower elevation. Analysis with the MRAMS mesoscale model shows very similar behavior (Rafkin et al., 2016). These arcs represent continuous paths along slopes in the domain and are discussed further in Section 5.3.

4.3. Removal of the tidal contribution to the diurnal pressure cycle

As described in Section 1, the focus of this study is the augmentation of the DRSP beyond that explicable by the genetic thermal tide. To examine the nature of this augmentation, we must therefore isolate its signature by removing the tidal component from the full pressure variation. If we assume that the surface pressure field associated with the synoptic scale thermal tides is uniform across the mesoscale Gale Crater region, then we can estimate the thermotidal contribution to the total daily pressure cycle as being the time-varying, $6° \times 6°$ spatial-average pressure:

$$P_{tidal}(t) = P_{spatial\ average}(t) - P_{daily\ and\ spatial\ average} \quad (1)$$

This is reasonable since the thermotidal contribution is dominated by the longest (synoptic scale) wavelengths (e.g., Wilson and Hamilton, 1996; Guzewich et al., 2016). Other synoptic motions that might be expected to influence the mesoscale area average (such as baroclinic systems that propagate into the tropics (e.g., Wang et al., 2003, 2005; Martinez et al., 2017)) contribute very little power on diurnal timescales and tend not to be harmonic with the diurnal cycle. The assumption of uniformity is also consistent with the relatively fast moving thermotidal mass perturbation conformably flowing over the mesoscale terrain at high Froude number (see Section 2.2.1).

The full pressure variation with local time is defined as the pressure minus the daily-averaged pressure at that location:

$$P_{full}(x, y, t) = P(x, y, t) - P_{daily\ average}(x, y) \quad (2)$$

The "non-tidal" variation is then the deviation of the full surface pressure variation from the tidal variation:

$$P_{non-tidal}(x, y, t) = P_{full}(x, y, t) - P_{tidal}(t) \quad (3)$$

The "non-tidal" terms at the landing site and at the summit of Aeolis Mons are shown in Fig. 1c. This Figure shows that the landing site (in red) experiences a "local" cycle of pressure deviation that is closely (but not completely) in phase with the large-scale tidal pattern (cf. Fig. 1b, green curve), while Aeolis Mons (in blue) experiences one that is close to being

fully out of phase with the large-scale tidal pattern.

The "full", "tidal" and "non-tidal" pressure contributions for a given site are more instructive when compared with each other on a single plot. In Fig. 5 we re-plot these terms for the Curiosity landing site (Fig. 5a) and the summit of Aeolis Mons (Fig. 5b), and additionally show sample sites on the flank of Aeolis Mons at intermediate elevation (Fig. 5c), on plains to the north of the dichotomy boundary (Fig. 5d), on the floor of a crater to the south of Gale (Fig. 5e), and in the southern highlands (Fig. 5f). The geographical distribution of these sites is shown on a topographic basemap in Fig. 5g.

Fig. 5a and b re-emphasize that at low elevation the non-tidal contribution acts to augment the DRSP, whereas at high elevation it acts to diminish it. In Fig. 5c, the site on the flank of Aeolis Mons experiences a daily surface pressure variation that is dominated by the thermal tide with almost no non-tidal surface pressure amplitude. The additional locations (Fig. 5d–f) were selected to test the generality of the elevation behavior for points outside of Gale Crater. Points to the north of the dichotomy boundary (Fig. 5d) and within a crater south of Gale (Fig. 5e) are close to the domain-average elevation, and also show a relatively weak non-tidal component. A point in the southern highlands on a local topographic maximum between two craters (Fig. 5f) experiences a relatively large non-tidal component that is again nearly 12 h out of phase with the thermal tide, similar to the findings at the Aeolis Mons summit. As a result, the 'full' pressure cycle at this location is significantly damped relative to the expectation from the thermal tide alone.

Although the impact of topography on local mass transport is given purely by the non-tidal component, Fig. 5a–f demonstrate that the magnitude of the PDRSP may be dominated by either the tidal or non-tidal component. Thus the non-tidal component on its own is a much better metric for the impact of topography on local mass transport than is the full PDRSP. To help visualize how the non-tidal pressure cycles vary spatially over the Gale Crater region, we show the non-tidal pressure perturbation at 15:00LT and 3:00LT in Fig. 5h and i, respectively. The very close relationship with topographic elevation is again highlighted. During the day (Fig. 5h), the non-tidal term generates negative pressure contributions over low terrain and positive pressure contributions over high terrain. Because the thermal tide itself has a minimum near this local time, the non-tidal component interferes constructively (destructively) with the thermal tide where the surface elevation is low (high). The opposite behavior is demonstrated at night (Fig. 5i). Thus across this whole region, the effect of the non-tidal perturbation is to augment the DRSP at lower elevations and to damp the DRSP at high elevations.

5. Proximity of the time-evolving surface pressure distribution to hydrostaticity

The spatial pattern of the relationship between PDRSP and elevation in Fig. 2a is diurnally and seasonally repeatable (Rafkin et al., 2016) and appears sufficiently simple that a first hypothesis is that it results from the surface pressure hydrostatically evolving in response to the daily air temperature cycle, as described in section 2.2.2.3. In this section, we provide a more quantitative assessment of how closely the surface pressure distribution adheres to hydrostaticity.

5.1. Definitions of hydrostatic and nonhydrostatic pressure distributions along a slope

The definition of hydrostaticity is a balance between gravity and the pressure gradient force directed along the gravity vector (see, e.g., Holton, 1992). The hydrostatic balance can be written as:

$$\frac{dP}{dz} = -\rho g = -\frac{Pg}{RT} = -\frac{P}{H} \quad (4)$$

where P is pressure, z is elevation, ρ is air density, g is acceleration due to gravity $= 3.74\ \mathrm{m\,s^{-2}}$ for Mars, T is local air temperature, R is the specific

gas constant ($=R^*/M$, where R^* is the universal gas constant and M is the molar mass of the Martian atmosphere, giving $R = 191.837 \, \mathrm{J \, kg^{-1} \, K^{-1}}$), and H is the scale height, $H = RT/g$. This equation yields the intuitive result that if the mean air temperature is increased, the scale height increases and the pressure drop between two fixed height levels decreases. If we consider only an isolated column (or a laterally uniform fluid undergoing laterally uniform heating), then this simply states that a heated column of air expands.

We can integrate this equation from some reference level (say the zero elevation datum, Z_0, at some reference surface pressure, P_0) in order to obtain the surface pressure for any given point, A:

$$\int_{P_0}^{P_A} \frac{dP}{P} = -\frac{1}{H} \int_{z_0}^{z_A} dz \tag{5}$$

yielding:

$$P_A = P_0 e^{-\frac{g(Z_A - Z_0)}{RT}} = P_0 e^{-\frac{(Z_A - Z_0)}{H}} \tag{6}$$

Where T is now the mean temperature of the layer between 0 and A, and H the scale height at this temperature.

Eqn. (6) is valid within a vertical column, but if we make the assumption that the air temperature is laterally uniform, then we can use this same relationship to compare the hydrostatic contribution to surface pressure at locations of different elevation along the slope. The purpose of doing this is that we would like to be able to examine what portion of the pressure difference between two points is merely due to the hydrostatic consequences of the points being at different elevation and to isolate this from the portion of the pressure difference that is due to dynamical processes. If the temperature varies laterally, then the scale height also varies. The effect of such lateral variation in temperature on the surface pressure is quantitatively described by Mahrt (1982) and is the slope-modified Sea Breeze circulation (Section 2.2.2.2). We will provide a much more detailed, quantitative comparison between the Sea Breeze and hydrostatic effects on surface pressure in Part 2 of this sequence of papers. Variations in the reference P_0 pressure can be associated with any imposed dynamical system that modifies the surface pressure and its gradient. For example, the global thermal tide is imposed upon the Gale Crater region and its signature, described in Section 4, modifies the absolute value of P_0. The tide is approximately horizontally uniformly on the scale of the Gale Crater system, and as such, though P_0 is not temporally fixed in this case, Eqn. (6) is valid to compare surface pressures for the same time. When a dynamical system on the same scale as the topography is imposed, P_0 could be interpreted as varying spatially, but the estimate based on a constant P_0 is still the desired calculation for isolating the purely hydrostatic lateral pressure field. In this case, there will be a difference between the hydrostatic estimate and the real surface pressure variation that can be used to isolate the dynamical from the hydrostatic contributions to surface pressure variation over complex topography.

Continuing from Eqn. (6), if we now consider two points along varied terrain (see the cartoon in Fig. 6a), we can calculate the surface pressure for each:

$$P_A = P_0 e^{-\frac{(Z_A - Z_0)}{H}} \tag{7}$$

$$P_B = P_0 e^{-\frac{(Z_B - Z_0)}{H}} \tag{8}$$

The difference in the surface pressure between the points is due to the fact that the points are at different surface elevations, and their relationship is given by:

$$P_A = P_B e^{\frac{(Z_B - Z_0)}{H}} e^{-\frac{(Z_A - Z_0)}{H}} = P_B e^{\frac{(Z_B - Z_0 - Z_A + Z_0)}{H}} = P_B e^{-\frac{(Z_A - Z_B)}{H}} \tag{9}$$

If we define the surface elevation difference between the points A and B as $\Delta z = Z_A - Z_B$, and we assume that the atmosphere is everywhere in
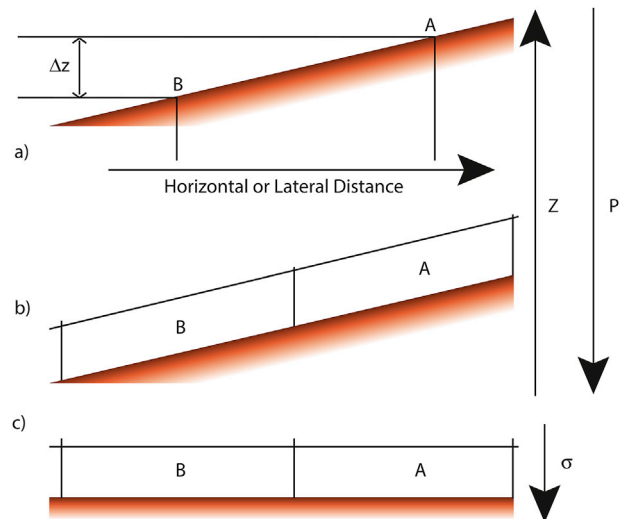

Fig. 6. **(A)** A cartoon of a vertical transect through an element of sloping terrain indicating the relative vertical and lateral displacements of Points A and B along the surface of the sloping terrain. **(b)** A cartoon of the discretization of the lowest model layer over sloping terrain projected in height vertical coordinates. **(c)** A cartoon of the lowest model layer in sigma coordinates.

hydrostatic balance at a mean temperature, T, and hence scale height, H, then the surface pressures at the two points A and B along the slope are related as:

$$P_A = P_B e^{-\frac{g\Delta z}{RT}} = P_B e^{-\Delta z/H} \tag{10}$$

Eqn. (10) is simply a rearrangement of the hypsometric relationship, which states that the height separation between two pressure levels is solely a function of the mean layer temperature between them (e.g., Holton, 1992). In the context of a slope, when we say that the along-slope pressure gradient is consistent with hydrostatic balance, we mean simply that the pressure difference between two fixed points along a slope is explained by the elevation difference between the points and the local scale height (hence the mean air temperature). Any deviation from such a hydrostatic pressure difference then means, by definition, that the deviation is laterally a nonhydrostatic pressure difference (i.e., that the pressure difference must be a signature of some dynamical process).

A potentially confusing issue is that numerical models are sometimes referred to as being "hydrostatic" or "nonhydrostatic" in construction. In this study, for example, MarsWRF is nonhydrostatic (as was MRAMS (Rafkin et al., 2016)), while MMM5 as run by Tyler and Barnes (2013, 2015) was hydrostatic. However, "hydrostatic" models are capable of generating slope-parallel "nonhydrostatic" pressure gradients. This is because – in all terrain-following vertical coordinate models – the projection of gravity along the slope enters the model horizontal momentum equations through the definition of a bottom boundary geopotential height that varies between grid points. The designation of a "hydrostatic" versus "nonhydrostatic" model refers only to whether *vertical* motion is diagnostic or prognostic and does not impact the horizontal (along slope) momentum equations. Thus, whether the model is hydrostatic along the z-axis (as is true in "hydrostatic" models) has nothing to do with whether the modeled atmosphere is out of hydrostatic balance laterally across varied terrain. For the dynamical systems under study in this paper, the insensitivity of the model results to the prognostic versus diagnostic treatment of the vertical momentum equation have been confirmed in two main ways: First, by comparing published "hydrostatic" MMM5 simulation output plots with those from the fully "nonhydrostatic" MarsWRF and MRAMS simulations (Tyler and Barnes, 2013, 2015; Rafkin et al., 2016); and second, by directly testing MarsWRF using

simulations in which the vertical momentum equation was changed from prognostic to diagnostic (not shown).

5.2. Estimation of proximity to hydrostatic balance along slopes

If the large daily variation of the surface pressure distribution is strongly controlled by lateral hydrostatic adjustment flows, then the surface pressure field at each instant ought to be very close to a state of lateral hydrostaticity across the varying terrain. We can test this by calculating a 'predicted pressure' at a given grid point using only the instantaneous near-surface air temperature, the surface pressure at an adjacent grid point, and the surface elevation difference between the two points, and then comparing this hydrostatically predicted pressure with the pressure predicted by the full numerical model.

Fig. 7 shows a single longitudinal slice along the middle of WithNests d04 (shown in Fig. 2a), centered on Gale Crater at latitude 4.5556°S, calculated for 15:00 and 03:00 local true solar time (LTST), *i.e.,* for day (left column) and night (right column) conditions. The pressure at each grid point along the slice is predicted from simple isothermal hydrostatic extrapolation from its western neighbor, using the elevation of the two grid points and the average of the near-surface air temperature between the two points. This diagnostic is simply a discrete form of Eq (10):

$$P_{predicted}[x] = P_{modeled}[x-1] * e^{\frac{-(z[x]-z[x-1])}{H\left[x-\frac{1}{2}\right]}}$$ (11)

where P is the pressure, x is the eastward grid point index, z is the elevation, where rounded brackets denotes mathematical grouping and square brackets reference evaluation of the variable at the specified location, and H is the scale height where:

$$H\left[x-\frac{1}{2}\right] = \frac{R(T[x]+T([x-1]))}{2g}$$ (12)

and T is the lowest model level air temperature. Note that while the hydrostatic relationship in Eqns. (4) and (11) can be derived from first principles, it can also necessarily be obtained from the full along-slope momentum equation (*e.g.,* Eqn. (28)) when the gravity and pressure gradient terms along the slope are dominant (*e.g.,* Holton, 1992).

The top row of Fig. 7 compares the surface pressure at each point (i) taken directly from the simulation (plus signs) and (ii) calculated from west to east using Eqn. (11) and the local simulated air temperature (crosses). To demonstrate the impact of using constant air temperatures rather than the local air temperature (note that the air and ground temperatures are shown in the bottom row of Fig. 7), the top row plots also show surface pressures calculated in the same way but now with one of three fixed air temperatures (180K is shown by the red line, 220K by the green line, and 260K by the blue line).

To emphasize how well the hydrostatic extrapolation works in terms of predicting the modeled surface pressure, the second and third rows show the difference between the model output and the hydrostatic prediction in terms of absolute and percentage pressure difference, respectively (*i.e.,* they show the difference between the pluses and crosses in the first row). The residual error is less than 0.5 Pa for most of the day and night. This corresponds to less than 5% piecewise error at all but a handful of points, with the average error less than 2%. We are thus left with the result that the atmosphere is in hydrostatic balance along the slope to about 98%, and therefore that nonhydrostatic deviations typically contribute something less than 2%.

This nonhydrostatic contribution can be visualized a little more clearly if we plot the integrated residual error in the surface pressure prediction. The red lines in the fourth row of Fig. 7 show the result of integrating the piecewise errors (shown in the second row) from west to east. From a definitional bias of 0 Pa on the western edge, Fig. 7g shows that the modeled surface pressure is higher than the hydrostatic prediction by about 5 Pa at the lowest point in the Gale Crater trough during the daytime, but that the integrated error returns to near zero at the eastern
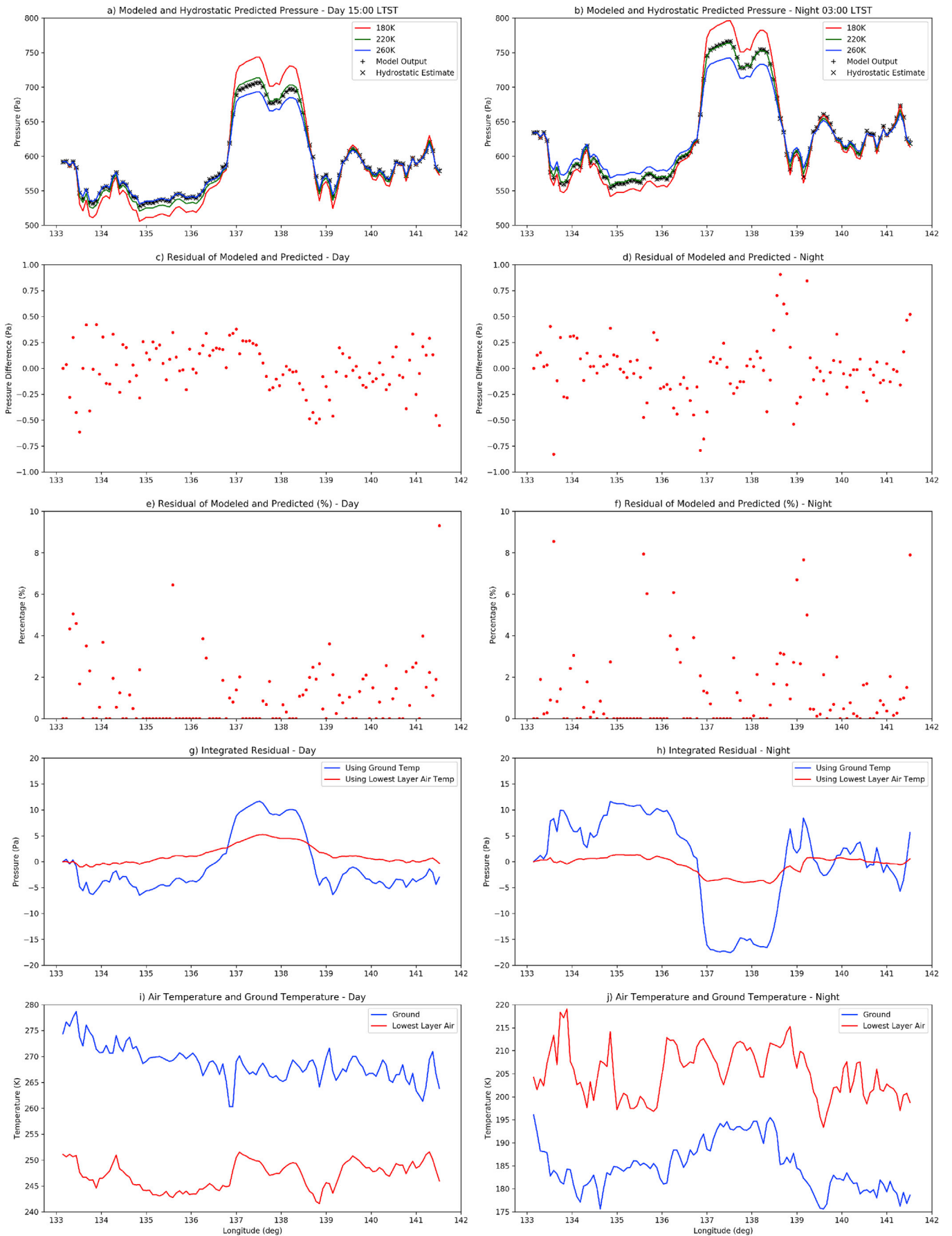
edge of the domain. At night, Fig. 7h shows that the integrated error again has no net bias across the whole domain, but that the modeled surface pressure is now lower than the hydrostatic prediction by about 5 Pa in the trough.

Fig. 7 thus shows that an atmosphere in complete hydrostatic balance along the slope would necessarily exhibit a DRSP at low elevations (such as the Curiosity landing site) that would be even larger than that produced by the numerical model. This follows from the fact that the total surface pressure is near its minimum during the day when the nonhydrostatic perturbation at low elevation is positive, and near its maximum at night when the low elevation nonhydrostatic perturbation is negative. The difference between the numerical model surface pressure distribution and the hydrostatic surface pressure distribution is definitionally due to the development of diurnally reversing nonhydrostatic pressure gradients in the model. The effect of nonhydrostatic lateral pressure gradients is thus to decrease (rather than amplify) the DRSP as measured by REMS. The nonhydrostatic surface pressure distributions that develop in the model are also consistent with those needed to accelerate flows that remove mass from the trough during the day (when the numerical model has too much mass in the trough relative to that needed for perfect hydrostaticity) and to fill it at night (when the crater trough has too little mass relative to hydrostaticity). Thus not only does the surface pressure distribution remain very close to hydrostaticity despite the wide diurnal range of near surface air temperature, but the nonhydrostatic distributions that do develop are of the correct structure to affect the necessary redistribution of air mass. The hypothesis that the surface pressure patterns can primarily be explained as being those needed to maintain hydrostatic balance is therefore confirmed – indeed lateral hydrostatic adjustment slightly over-explains the Curiosity DRSP, and small nonhydrostatic pressure gradient effects are needed both to explain the acceleration of the required lateral hydrostatic adjustment flow and to slightly reduce the low elevation DRSP.

The influence of the temperature choice in Eqn. (12) is also illustrated in Fig. 7g and h, with the blue lines showing the impact on the integrated error of using surface temperature rather than lowest-layer air temperature. Note that the integration does not return to zero at the eastern edge of the domain and that the predicted nonhydrostatic pressure variations over Gale Crater are much larger than generated using the air temperature in the lowest model layer (shown by the red lines). In the discrete numerical model, the latter is the obvious choice, because it is this temperature that is used in the MarsWRF lowest layer horizontal momentum equation. However, this choice is less obvious in the case of the real continuum atmosphere. Even in the model the choice is indirectly problematic in that the predicted values of air temperature in different simulations depends upon the choice of the vertical grid spacing used. The real physical mechanism obviously cannot have a dependence on numerical grid choice. This is a topic to which we shall return in Part 2 of this sequence of papers.

5.3. The importance of lateral air temperature variations and lateral "interconnectedness"

Different areas of terrain exhibit different diurnal air temperature cycles due to variations in surface thermal properties and as a result of a range of dynamical processes, as discussed in much greater depth by Tyler and Barnes (2013; 2015) and Rafkin et al., (2016). Such lateral variations are evident in the daytime and nighttime air temperatures, shown in the bottom row of Fig. 7 and in map form in Fig. 8. These variations influence the hydrostatic balance state to which the along-slope pressure gradients are driven. We have previously noted that the spatial variation of near-surface air temperature at a fixed local time (about 5–10 K in Fig. 7) is much smaller than the daily variation of the near surface air temperature (about 40 K in Fig. 7). Fig. 8a–c shows the daily variation across the whole region is likely larger than sampled in Fig. 7, at nearer 55–65 K. As a result, the modification of the surface pressure field generated by these lateral variations in air temperature is

(caption on next page)

Fig. 7. Longitudinal variation of pressure and temperature across the central latitude of WithNests d04 (the domain shown in Fig. 2). The latitude along this transect is 4.5556°S. Two local times are shown: **(left column)**: 1500 LT (3pm) and **(right column)**: 0300 LT (3am). **(a)** and **(b)**: Surface pressure (Pa) from (pluses) the MarsWRF simulation and (crosses) calculated from left-to-right as a piecewise hydrostatic extrapolation from the prior point and at the local air temperature. Colored lines correspond to reference hydrostatic extrapolations at constant temperature from the extreme left-hand point at (bottom to top) 180, 220, and 260 K. **(c)** and **(d)**: The residual of the MarsWRF model and the piecewise isothermal hydrostatic extrapolation (Pa) on a gridpoint-by-gridpoint basis. **(e)** and **(f)**: The residual difference (from c and d) shown as a percentage of the total difference in pressure between adjacent grid points. The quantity is effectively the percentage error resulting from the piecewise hydrostatic extrapolation. Where the horizontal change in pressure between MarsWRF grid points is less than 5 Pa, the percentage has not been calculated since for small denominators the percentage calculation becomes very noisy (note that 'zeroed' percentages tend to be associated with absolute pressure error values of <0.5 Pa). **(g)** and **(h)**: The cumulative residual calculated by summing the individual residuals (from c and d) starting from a zero value at the extreme left of the domain. To the extent that the residuals represent real nonhydrostatic effects rather than 'noise' (numerical or turbulent), the cumulative residual shows the effective distribution of the nonhydrostatic perturbation surface pressure distribution across the domain. Since the choice of zero is arbitrary, the values are only of meaning in a relative sense across the transect. However, note that the signatures of the strong slopes within Gale Crater are clearly evident as perturbation high pressures during the day and as perturbation lows during the night. The red curve uses the lowest layer atmospheric temperature in the hydrostatic estimation while the blue curve uses the ground temperature. **(i)** and **(j)**: The lowest layer air temperatures (red curve) and ground temperatures (blue curve). (For interpretation of the references to colour in this figure legend, the reader is referred to the Web version of this article.)

secondary to the influence of the diurnal variation of air temperature, although their effect can still be seen in the model output. The relatively small spatial variation, and equivalently its second order role, result from the lack of strong surface thermal property contrasts within the Gale Crater region (ground temperature daily minima, maxima, and range are shown in Fig. 8d–f), from the fact that the mesoscale extent of the region means that there is negligible impact of sun-angle (local time or latitude) variations on heating across the domain, and from the fact that radiative-convective heating of the air is more important than dynamical heating. The influence of lateral thermal variations upon the lateral hydrostatic pressure distribution is more important at synoptic and seasonal scales on Mars. We revisit this topic in Part 3 of this sequence of papers.

The degree to which lateral air temperature variations modify the PDRSP's dependence on surface elevation is shown in Fig. 9. Each of these transects (Fig. 9b, d, and f) is a limited portion of the distribution shown in Fig. 2b. Fig. 9a shows elevation for the same west-to-east slice across Gale Crater shown in Fig. 8, while Fig. 9c and e shows transects that pass directly over the summit of Aeolis Mons in the east-west and north-south directions, respectively. Fig. 9b, d and 9f show the modeled PDRSP as a function of elevation at all points along each of the transects. Since the lines in Fig. 9b, d and 9f are all continuous with distance along the transects, all three show trajectories along the surface. Given the limited range of elevation sampled (for example, elevations below −4 km are only sampled within Gale Crater, while elevations below −2.5 km are sampled within both the crater and the lowlands to its immediate south and east), it is relatively easy to see how the PDRSP varies with elevation along distinct subsections of the continuous trajectories. For clarity we label significant topographic features and the starting and ending points of each transect.

Fig. 9b and d shows only two major "limbs" of the PDRSP vs. elevation trajectory. The lower limb corresponds to the flanks of Aeolis Mons and the interior walls of Gale Crater, while the upper limb corresponds to the plains to the east of Gale Crater. In both areas, the PDRSP vs. elevation trajectories are both very smooth and very nearly monotonic, but with the gradients and intercepts of the two trajectories differing from each other. Examination of Fig. 8a–c suggests that, compared to the interior of Gale Crater, the plains to the east are significantly cooler at night and have a larger daily range of air temperature. The latter requires a larger PDRSP change with elevation (explained in more detail in the next Section), and indeed, the upper 'limb' in Fig. 9b (corresponding to the plains) generates a PDRSP variation of about 4% (from 6 to 10%) for a roughly 1750 m elevation change, while the somewhat smaller air temperature cycle inside the Gale Crater system requires over 3000 m of elevation change to generate the same PDRSP change.

The north-south profile across the domain (Fig. 9f) shows even more fragmentation of the PDRSP vs. elevation behavior into distinct coupled regions. While the slopes of Aeolis Mons and the inner slopes of the crater rim roughly overlay each other, outside Gale Crater there is a clear north/south asymmetry. North of the crater, the points largely sit along several

overlaying trajectories with an intercept below that of the crater interior trajectories. This is a region with a smaller daily air temperature cycle than within the crater, and a small range of elevation changes. South of the crater, conversely, the points sit along three to five clearly distinct trajectories, the gradients of which are steeper on south-facing vs. north-facing slopes, and all of which have higher intercepts than those within the crater. The association of steeper gradients with south-facing slopes points to a larger diurnal range of air temperatures above these south-facing slopes. The region south of Gale Crater has a relatively large daily cycle of air temperatures and a significant amount of elevation change.

The suggestion from Fig. 9 is thus that the idea of the PDRSP as a simple function of elevation is only valid within dynamically connected regions of limited extent. The PDRSP vs. elevation function is not globally unique in that it depends upon the local daily average and range of air temperature, upon the PDRSP behavior in neighboring regions (*i.e.,* the function along one slope is constrained to agree at the peak or trough where it joins a neighboring slope), and upon the relative importance of along-slope gravitational acceleration within the lateral momentum equations (*i.e.,* upon the slope angle). This is discussed further in Section 6.4 and 6.5.
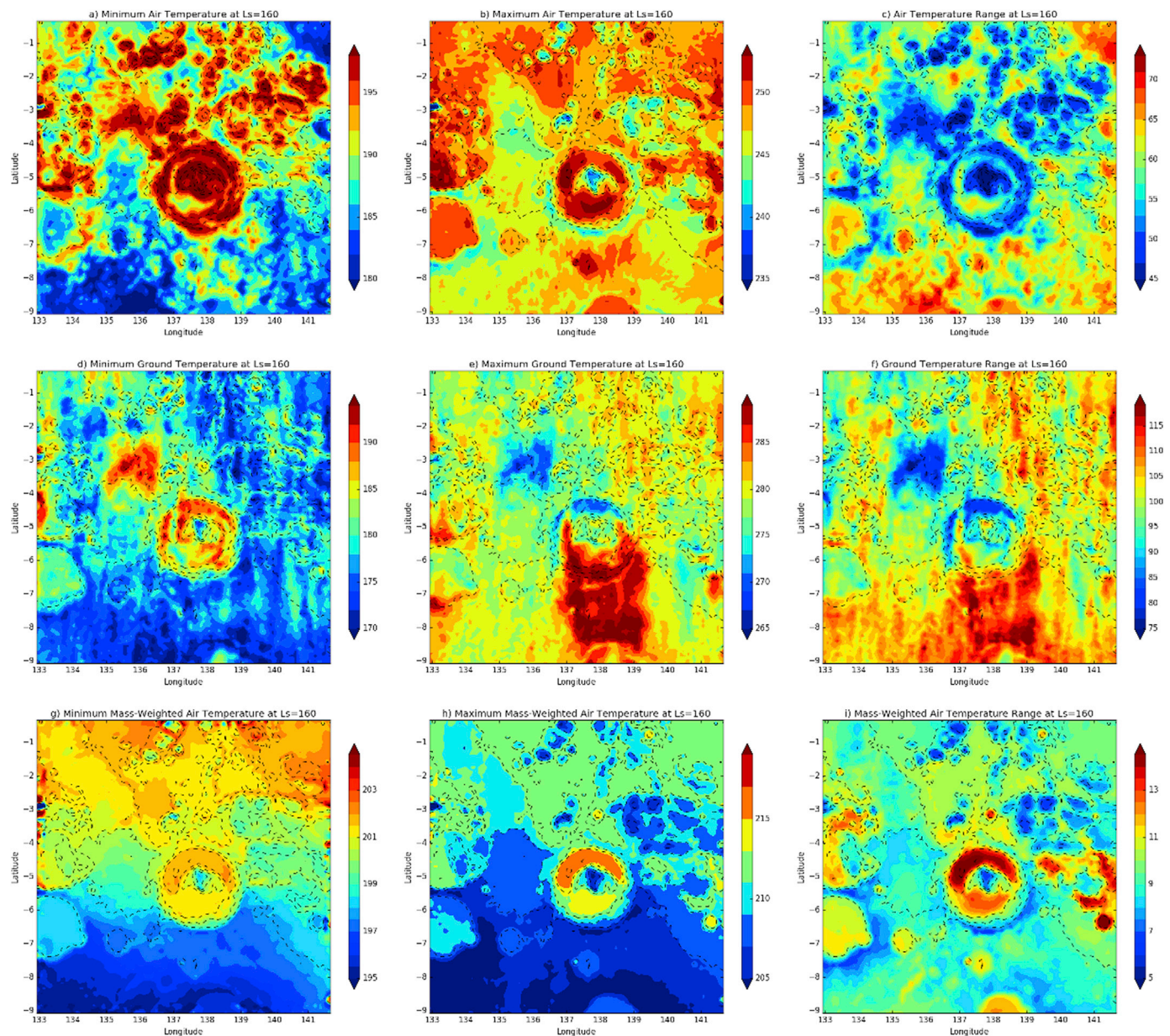
Note that here we benefit from examination of only a small (mesoscale) region around Gale Crater within which we can consider the thermotidal contribution to the PDRSP to be laterally uniform. Any lateral variation of the PDRSP over the limited Gale Crater area can therefore be uniquely ascribed to variation in the non-tidal, mesoscale mass-redistributive flow contribution (and hence to the lateral hydrostatic adjustment process, as described in the next Section). However, thermotidal contributions do become important as we consider synoptic scale domains (see, *e.g.,* Fig. 5 in Guzewich et al., (2016)). Thus, full PDRSP cannot naively be employed as a diagnostic of the relative importance of mesoscale mass-redistributive circulations across widely separated locations on Mars. Since the use of the full PDRSP would increasingly alias and confuse the spatial pattern of the tidal contribution to PDRSP with that of the non-tidal contribution as the scales examined become larger, a global equivalent of the non-tidal pressure variation, modified from Eqns (1)–(3), is needed for such purposes. This is defined and described in detail in Part 3 of this sequence of papers.

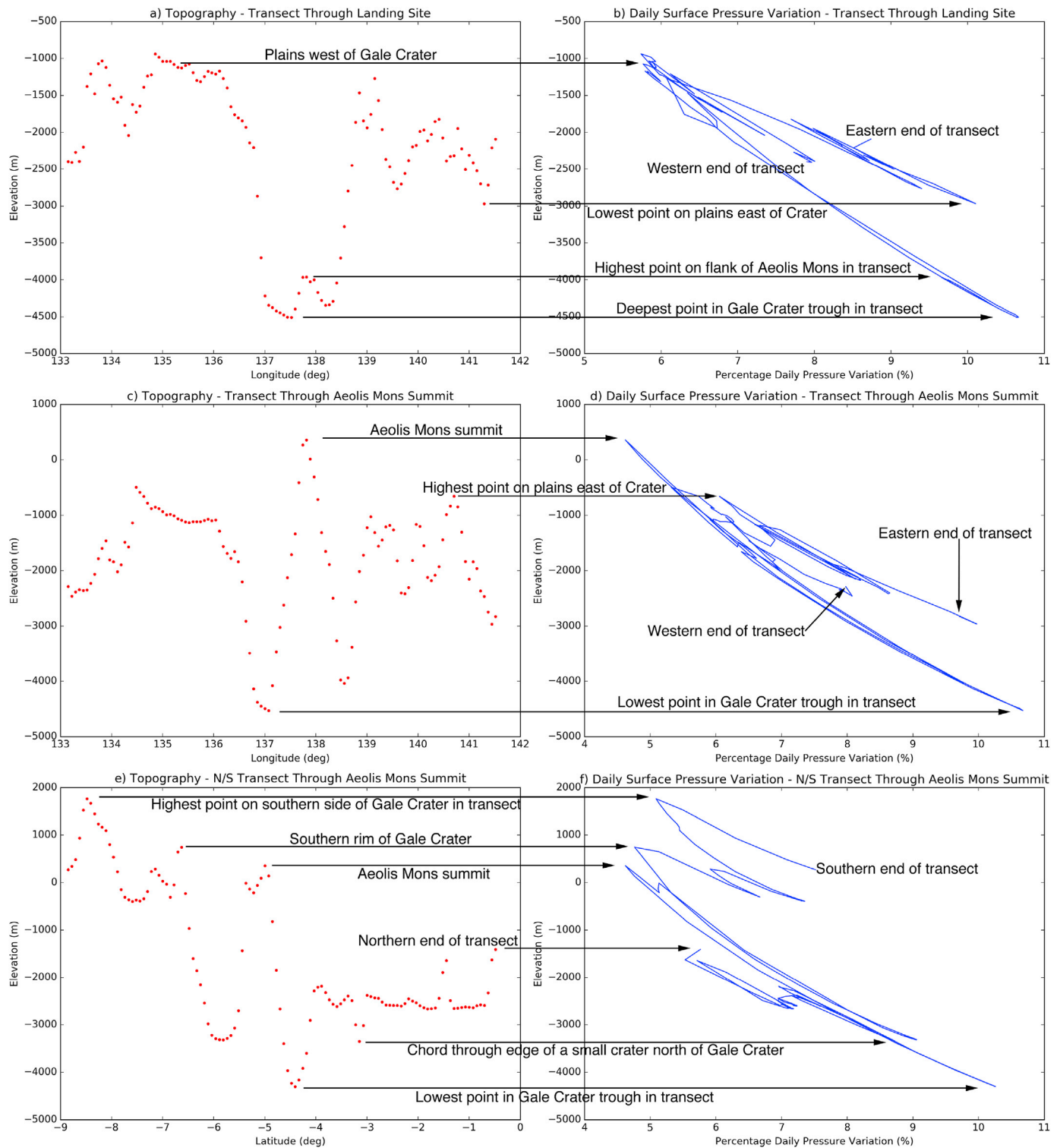## 6. The hydrostatic adjustment flow

The analyses presented in Sections 4 and 5 suggest that the PDRSP augmentation at the Curiosity landing site results from the redistribution of atmospheric mass needed for the atmosphere to remain close to hydrostatic balance over the diurnal thermal cycle. Specifically, the prior sections demonstrated that:

1. The augmentation of PDRSP at the Curiosity landing site is unambiguously associated with conservative mass-redistribution over the mesoscale topography of the Gale Crater region and forced by the daily cycle of air temperatures (Section 4);

2. The non-tidal daily surface pressure cycle at any location within the Gale Crater region differs characteristically depending on the surface elevation for that location relative to the domain average (Section 4);

3. The lateral variation of surface pressure across the broad range of terrain is always very close to a state of local lateral hydrostaticity, *i.e.,* the surface pressure at any point can very accurately be predicted from that of an adjacent location based solely on the elevation difference between the locations and the local, near-surface air temperature (Section 5);

4. Close hydrostaticity is maintained despite a very large daily cycle of air temperature and hence of the scale height (see Section 5).

In this section, we explore the dynamics of an idealized atmosphere over sloping terrain as the mean air temperature changes. We focus on a mesoscale system of fixed total mass, which is applicable to the Gale Crater regional surface pressure after the thermotidal contribution is removed (Section 4). Specifically, we expand quantitatively upon the description of the hydrostatic adjustment flow presented in Section 2.2.2.3. We show how the surface pressure distribution along a slope varies with the mean air temperature and results in the different local-time phasing of the surface pressure cycles at low and high relative surface elevations. For an approximately hydrostatic atmosphere, we provide a means of estimating the size of the PDRSP augmentation based on the surface elevation difference and the magnitude of the air temperature cycle. We describe how hydrostaticity along the surface of sloped mesoscale terrain results from the tendency of the lateral pressure gradient force to balance the projection of gravity along the slope, and for these two forces to dominate the along-slope momentum equation.

Fig. 8. Maps of the daily minimum, daily maximum, and daily range of temperature from d04 for **(a–c)** the lowest model level air temperature, **(d–f)** the ground temperature, and **(g–i)** the mass weighted whole column air temperature. Dashed lines on all panels are contours of topography and are included to provide reference for the locations of Gale Crater, Aeolis Mons, and other topographic features within the Gale Crater region (*c.f.*, Fig. 5g).

Fig. 9. Three transects across the Gale Crater d04 domain are shown to illustrate the relationship between **(left)** topography and **(right)** the PDRSP. Transects are **(a)** and **(b)** east-west across the Curiosity landing site (at 4.5556°S), **(c)** and **(d)** east-west across the summit of Aeolis Mons (5°S), and **(e)** and **(f)** north-south across the Aeolis Mons summit (137.8°S). For the PDRSP, the values at the model grid points are joined by blue straight-line segments to emphasize the continuous path along each model transect. For both zonal transects (a–d), the majority of the domain follows essentially the same (lower) trajectory in the plot phase space. The upper limb or trajectory is followed as the transect descends to the lowlands at the extreme east of the model domain. For the meridional transect, there is a distinct shift of the curve between the southern edge of the domain and the southern edge of Gale Crater. The differences in PDRSP result from the different thermal behavior across the domain (see Fig. 8). Major topographic features corresponding to points along the three topographic curve are indicated and labeled. (For interpretation of the references to colour in this figure legend, the reader is referred to the Web version of this article.)

Finally, we provide a quantitative description both of the imbalance between the two forces created by changes in the air temperature and of the resulting flow that laterally transports net mass in order to restore the balance.

6.1. A conceptual model of hydrostatic adjustment over large terrain

In order to see why the surface pressure distribution along slopes must change as the air temperature is varied, consider the behavior of isobaric surfaces over a smooth, uniformly sloping surface, and within an idealized atmosphere that is isothermal in all three spatial dimensions and initially at rest (see Fig. 10). These assumptions allow us to dispense with complexities that are of secondary importance yet provides a quantitative description of the evolving surface pressure distribution that explains all of the major features highlighted in Sections 4 and 5 (these complexities are reintroduced in Part 2 of this sequence of papers).

We will initially consider two fixed locations along the surface of the slope shown in Fig. 10: point A at high elevation and point M at lower elevation. For conceptual simplicity, we will require the surface pressure at point M to remain at a fixed value, P_M, and examine what happens to the surface pressure at point A, P_A, as the spatially-uniform air temperature is varied in time. Note that P_U and P_L are the constant pressures of an upper and lower isobaric surface. We start at the coolest time of day and slowly increase the temperature such that the atmosphere remains infinitesimally close to hydrostatic balance (an animated version of this system is shown as a movie in the supplementary materials; Supplementary video related to this article can be found at https://doi.org/10.1016/j.pss.2018.07.003). The temperature is changed sufficiently slowly that any dynamical heating is small compared to radiative damping, and we need examine only the slow, net motions. As the air temperature increases, the scale height will also increase, *i.e.,* the atmosphere will expand. By the hypsometric relationship, Eqn. (10), this means the vertical level of the P_U isobaric surface that initially intersects the slope at a lower elevation than that of point A will move upwards to intersect the surface at a higher elevation than that of point A. This corresponds to an increase in surface pressure at point A. As we get to our maximum "warm state" value of air temperature, point A is at a pressure between P_U and P_M (*i.e.,* $P_M > P(A) > P_U$).

If we were to cycle the air temperature through a daily cycle starting and returning to our initial value, then in order to remain in hydrostatic balance with the fixed surface pressure at point M, the surface pressure at point A would necessarily also execute a daily cycle driven by and in
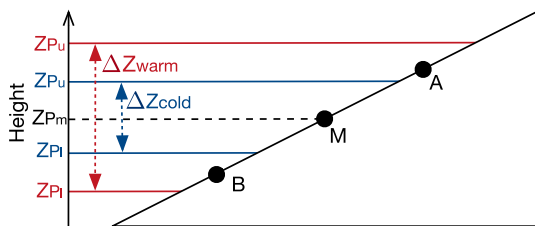
phase with the air temperature (see the movie included in the Supplementary Materials). Note that this cycle is only required because points A and M are located at different elevations along sloping terrain that cuts across horizontal isobaric surfaces and because the separation of these isobaric surfaces is controlled by hydrostaticity.

Considering the varying surface pressure at point A relative to a fixed surface pressure at point M is conceptually useful as it allowed us to focus on the influence of the upward displacement of the P_U isobaric level upon the actual surface pressure at point A. However, an isolated domain with only points A and M does not conserve mass, by design, since we only allow surface pressure changes that are either everywhere positive (when warmed) or everywhere negative (when cooled) along the slope and since everywhere on the slope is at an elevation higher than at point M. Hence this idealized system does not provide a useful physical framework within which to examine the flow needed to actually change the surface pressure at point A.

For a more realistic model of the system in the Gale Crater region, we additionally consider a point B at an elevation along the slope that is lower than that of point M. Within this domain containing points A, B, and M, we now also require the total mass to be conserved. This simple domain provides a useful initial model for thinking about the mesoscale flow interior to the Gale Crater region after the synoptic scale daily variation of surface pressure has been removed (Section 4). Point M is chosen to be at the location where surface pressure does not change and hence at an elevation where the surface pressure equals the area weighted domain average surface pressure. By definition, this also corresponds to the location where the isobaric surface that has the same value as the domain mean pressure (P_M) intercepts the sloping ground. If we now consider an increase in the mean air temperature, a surface pressure increase at point A must be balanced by a surface pressure decrease at point B, and vice versa. Since an increase in surface pressure at point A requires an increase in mass per unit area in the column above point A, and the decrease in surface pressure at B requires a decrease in the mass of air above B, the compensating changes in surface pressure corresponds to a mass conservative movement of air from point B to point A. Thus, the dynamical origin of the flow can be considered as arising from the need to both conserve mass within the domain and to allow points A and B to attain their necessary surface pressure so as to satisfy the hypsometric relationship as temperature evolves.

6.2. Slope hydrostaticity and the forces acting on an air parcel

Hydrostaticity has thus far been used in the context of the vertical separation of isobaric surfaces that intercept sloping terrain, but it is also possible to examine the forces on a notional air parcel at the surface of a slope and within a coordinate system rotated parallel to the slope (see Fig. 3). The two approaches are formally equivalent if the atmosphere is always very close to a state of hydrostatic balance as the air temperature varies, which was demonstrated to be the case for the atmosphere over the Gale Crater region in Section 5. If we assume that projection of gravity and the pressure gradient force along the slope balance each other and that other forces are negligibly small (we examine the size of these secondary forces in Section 6.4), then from the hydrostatic relationship (Eqn. (4)) and the definition of the slope angle, α, (*i.e.,* where $\sin\alpha = \partial z/\partial s$, and where s is the distance along the slope in the uphill direction), we can write the along-slope balance of forces acting on the parcel as:

$$\frac{\partial P}{\partial s} = -\rho g \sin \alpha \tag{13}$$

Using the ideal gas law, $\rho = P/(RT)$, we can rearrange to yield:

$$RT \frac{\partial \ln P}{\partial s} = -g \sin \alpha \tag{14}$$

The forces acting on an air parcel are perhaps most intuitively thought

Fig. 10. Schematic illustration of how the elevation of isobaric surfaces change as the temperature changes from cold (blue lines and text) to warm (red lines and text) in a hydrostatic closed system along a slope. Points A and B are discussed in the text and are representative points above and below the point M on the slope corresponding to the elevation at which the domain mean pressure intercepts the surface. P_l and P_u are arbitrary pressure levels located at lower and higher altitudes than the domain mean pressure, P_m, respectively. Note that due to the decrease of pressure with increasing height, the "lower" level has a greater pressure value than the "upper" layer (*i.e.,* $P_l > P_m > P_u$). The absolute elevation (geopotential height) of the lower and upper pressure levels is designated by z_{Pl} and z_{pu}, while the height separation between the P_l and P_u levels is designated for the warm atmosphere by Δz_{warm} and for the cold atmosphere by Δz_{cold}. A modified and animated version of this figure is provided in the Supplementary Materials. (For interpretation of the references to colour in this figure legend, the reader is referred to the Web version of this article.)

of in terms of a change in density. It is easiest to examine a parcel at point M (Fig. 10), where the pressure is defined to remain constant and the density is thus solely determined from the air temperature via the ideal gas law. Balance is maintained upon the slope if the magnitude of the pressure gradient, $|\partial P/\partial s|$, decreases as the density decreases, and vice versa. The nature of the balance is evident from consideration of Eqn. (13), where the left hand side (LHS) corresponds to the pressure gradient force per unit volume of air and the RHS to the weight of the air per unit volume. This weight of the parcel due to the action of gravity upon the parcel mass density tends to pull the parcel down the slope, and at equilibrium the difference in pressure between the downhill side and uphill side of the air parcel is just sufficient to hold it in place. This difference of pressure across the parcel corresponds to the equilibrium hydrostatic surface pressure distribution, which can be found from the along-slope integration of Eqn. (14).

If the parcel density is changed, the balance is thrown off. If the density is reduced, the pressure difference across the parcel is too large and the parcel will accelerate uphill. If the parcel density is increased, the pressure differential will be too small and the parcel will accelerate downhill. However, it is important to note that the sign of these lateral accelerations results in a mechanism that is always restorative of an equilibrium surface pressure gradient. Specifically, an imbalance induced by a change of the mean density accelerates a mass flow that adjusts the pressure gradient field towards balance with the new mean density. In the case of a density decrease, the resulting flow of air uphill tends to increase the mass per unit area at higher elevations along the slope and to decrease it at lower elevations. Since pressure will always decrease with altitude in a Mars-like atmosphere on meso- and synoptic scales, this direction of mass transport always results in a decrease of the surface pressure gradient. In the case of a density increase, the flow of mass downhill thus similarly always leads to an increase of the surface pressure gradient. The acceleration of this stabilizing lateral hydrostatic adjustment flow is quantified in Section 6.4.

Note also that the drive for motion has nothing to do with spatial density perturbations. In our idealized case, we have spatially uniform changes in density associated with a fully (isotropically) isothermal change in temperature. As such, the force generating the motion is not associated with the genetically-defined immersion buoyancy force (see Section 2.2.2.1 and Part 2). Instead, the force driving motion is caused by a change in the pressure gradient force, $1/\rho(\partial P/\partial s)$, due to the change in the spatial-mean density.

6.3. Temporal evolution of the hydrostatic surface pressure distribution along a slope

The imposition of an air temperature variation within a hydrostatic atmosphere over sloping terrain was shown to require a change of the along-slope surface pressure distribution and to naturally accelerate a flow necessary to accomplish the mass redistribution (Sections 6.1 and 6.2). Fig. 11 provides a cartoon illustration of how the surface pressure at points A and B, shown in Fig. 10, responds if the temperature change is introduced as a simplified diurnal cycle (Fig. 11a) and assuming that the atmosphere adjusts instantaneously to the evolving hydrostatically balanced state. The surface pressure cycle at point A (Fig. 11b) is in phase

with this thermal signal. This happens because the separation between the height of the P_U surface and the P_M surface (Fig. 10) must increase as the temperature increases and thus the P_U pressure level must move upward and hence the surface pressure at point A must increase. However, the separation between P_M and the P_L level must also increase as air temperature increases, and given that the absolute height (and position of the intercept point, M, on the slope) cannot change, the height of the P_L level must decrease. This puts the P_L level below the height of the slope at point B, which means that the pressure at the surface at point B must be less than P_L. This corresponds to the surface pressure at point B decreasing as the temperature increases, and means that the diurnal cycle of pressure at point B (Fig. 11c) is out of phase with the air temperature cycle.

We provide a more quantitative description of how the surface pressure varies at the different locations on the slope by defining a functional form for the air temperature cycle. A simplified example is provided by a cosine wave, which has the property of starting from the coldest portion of the cycle, consistent with the discussion in Section 6.1:

$$T(t) = T_0 + T_1 \cos(t + \pi) \tag{15}$$

where t is in units of radians with one complete circuit representing a day, and the daily temperature amplitude, T_1, is assumed to be small compared to the daily average air temperature, T_0 (here and throughout this paper we use the standard definition of "small" such that x is small relative to y if x is roughly an order of magnitude or more smaller than y). The time evolving surface pressure at point A can be found from the fixed surface pressure at point M, using Eqn. (10), as:

$$P_A(t) = P_M e^{-\frac{g\Delta z}{RT(t)}} = P_M e^{-\Delta z/H(t)} \tag{16}$$

Substituting T(t) from Eqn. (15) into Eqn. (16) and using a series expansion for $1/(1 + x)$, Eqn. (16) can be approximated to first order as:
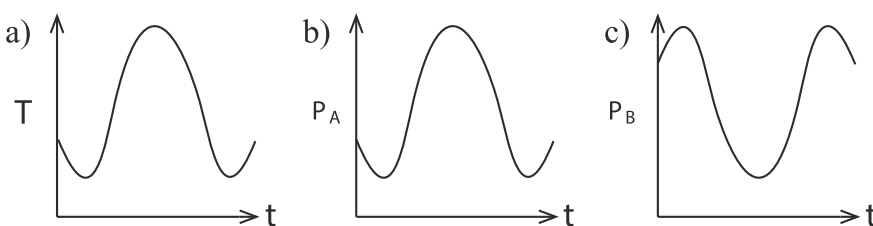
$$P_A(t) \approx P_M e^{-\frac{\Delta z}{H_0}} e^{\frac{\Delta z}{H_0}\frac{T_1}{T_0}\cos(t+\pi)} = P_A(0) e^{\frac{\Delta z}{H_0}\frac{T_1}{T_0}\cos(t+\pi)} \tag{17}$$

where H_0 is the scale height at temperature T_0, and $P_A(0)$ is the surface pressure at point A and at time $t = 0$. We can proceed to simplify Eqn. (17) further by using a series expansion for e^x and again retain only to first order:

$$P_A(t) \approx P_A(0)\left(1 + \left(\frac{\Delta z}{H_0}\right)\left(\frac{T_1}{T_0}\right)\cos(t + \pi)\right) \tag{18}$$

Eqn. (18) shows that when point A is located above point M on the slope (i.e., when $\Delta z > 0$), a periodic temperature oscillation generates a periodic cycle of the surface pressure that is in phase with the air temperature cycle. If the label 'A' is replaced in Eqn. (18) with the label 'B', and the value of Δz is set to be negative (implying an elevation below that of point M), then the surface pressure cycle at point B is found to be 12 h out of phase with that of the air temperature cycle. The trends are consistent with those sketched in cartoon form in Fig. 11.

The idealized behavior described by Eqn. (18) and in cartoon form in Fig. 11 is clearly reminiscent of that in the MarsWRF mesoscale output once the synoptic scale tidal signature is removed (Fig. 1c and red crosses in Fig. 5a–f), i.e., after net daily movements of air mass into and out of the

Fig. 11. Schematic illustration of how **(a)** near surface air temperature varies with local time and how this drives pressure changes at **(b)** Point A at an elevation along a slope above that of the domain mean pressure, and **(c)** Point B at an elevation on a slope below that of the domain mean pressure. See Fig. 10 for reference (points A and B are the same as those used in Fig. 10) and Section 5 for more details. The idealized pressure curves in panels (b) and (c) should be compared with the "non-tidal" pressure contributions in Fig. 5a–f.

mesoscale Gale Crater region are subtracted (Section 4). In particular, the behavior at points A and B (Fig. 11b and c) should be compared with the curves shown in Fig. 1c for the landing site (red) and summit of Aeolis Mons (blue), and which are also shown as the "non-tidal" components in Fig. 5a and b. The "non-tidal" component shown in Fig. 5c corresponds closely to the expected behavior described for point M. Specifically, to first approximation the nature of the DRSP augmentation at the Curiosity site corresponds to the low elevation (point B) diurnal cycle that constructively interferes with the thermal tide, while the DRSP damping expected for the summit of Aeolis Mons corresponds to the high elevation (point A) diurnal cycle that destructively interferes with the thermal tide.

6.4. Estimating the DRSP augmentation from non-dimensional analysis

An estimate of the DRSP at two points along the slope can be made by considering points A and B along the slope in Fig. 10. At any given time, the relationship between the pressure at point A, P_A, and that at point B, P_B, is provided by Eqn. (10). We will assume that both points are representative of locations of equal area. Let us consider two different times at extrema of the diurnal cycle, times 1 and 2 with uniform, isothermal temperatures T_1 and T_2, and hence with scale heights H_1 and H_2, yielding surface pressures at point A of $P_A(1)$ and $P_A(2)$, and likewise for point B. The DRSP at point A is:

$$\Delta P_A = P_A(1) - P_A(2) = P_B(1)e^{\frac{\Delta z}{H_1}} - P_B(2)e^{\frac{\Delta z}{H_2}} \tag{19}$$

while that at point B is

$$\Delta P_B = P_B(1) - P_B(2) \tag{20}$$

To simplify the analysis further, we can examine the regime in which the topographic range, Δz, is small compared to the scale height, H, in which case we can expand the exponents as a series and neglect all terms of order Δz^2 or higher. Eqn. (15) then simplifies to:

$$\Delta P_A \cong P_B(1)\left[1 - \frac{\Delta z}{H_1}\right] - P_B(2)\left[1 - \frac{\Delta z}{H_2}\right] = \Delta P_B - \frac{P_B(1)\Delta z}{H_1} + \frac{P_B(2)\Delta z}{H_2} \tag{21}$$

If we then further assume that the DRSP is small relative to the daily mean pressure, then $P_B(mean) \approx P_B(1) \approx P_B(2)$, and:

$$\Delta P_A \cong \Delta P_B - P_B(mean)\Delta z\left[\frac{1}{H_1} - \frac{1}{H_2}\right] = \Delta P_B - P_B(mean)\Delta z\left[\frac{H_2 - H_1}{H_1 H_2}\right] \tag{22}$$

Again, in the limit of perturbations in which the difference between T_1 and T_2 is small relative to the average of T_1 and T_2 (and hence likewise for the scale heights), we arrive at an approximation to the relationship for the DRSP variation across a slope:

$$\Delta P_B - \Delta P_A \cong P_B(mean)\left[\frac{\Delta z}{H_{mean}}\right]\left[\frac{H_2 - H_1}{H_{mean}}\right] \tag{23}$$

Neglecting the higher order terms thus gives us a very useful quantitative gauge of how the DRSP is expected to vary along a slope. Eqn. (23) shows that the difference in the ranges ($\Delta DRSP = \Delta P_B-\Delta P_A$) is proportional to: (1) the height of the terrain relative to the average scale height (a non-dimensional height of the terrain, $Z = \Delta z/H_{mean}$), and (2) the difference in the scale height induced by the daily thermal cycle relative to the average scale height (a non-dimensional measure of the daily cycle of air temperature, $\Theta=(H_2-H_1)/H_{mean}= (T_2-T_1)/T_{mean}$), i.e.,:

$$\Delta DRSP = P_{mean}*Z*\Theta \tag{24}$$

and

$$P\Delta DRSP = \frac{\Delta DRSP}{P_{mean}} \times 100 = [Z*\Theta] \times 100 \tag{25}$$

where PΔDRSP is the percentage difference in the daily range of surface pressure across terrain of non-dimensional height difference Z and non-dimensional diurnal temperature range Θ.

We can see from Eqn. (25) that if $Z \sim 0$ we recover the obvious result that when there is no topographic elevation difference, we expect no lateral variation in the DRSP. This also suggests that while we need to pay attention to topographic variations on scales of O (>100 m) for a scale height of roughly 10 km on Mars, we do not need to worry about hydrostatic slope flow over mounds of O (<100 m), for example. Likewise, if the daily thermal cycle is sufficiently small that the difference in scale height between day and night is negligible compared to the mean scale height, and hence the non-dimensional daily temperature range, $\Theta \sim 0$, then we again do not expect any along slope variation in the DRSP. For example, if a region has a mean temperature of 200 K and a 2 K diurnal temperature range, this would correspond to $\Theta = 0.01$, which we would not need to consider. However, the diurnal temperature range is usually much larger than this on Mars, thus there will typically be a noticeable along-slope variation in DRSP over significant mesoscale topographic relief. On Earth, with a much smaller typical diurnal air temperature range, a larger value of g, and a generally smaller range of topographic variation, the variation of DRSP over mesoscale topographic relief is generally less notable.

If we put numbers into Eqn. (25) for the ranges of interest at Gale Crater, we can use a diurnal air temperature cycle of 40 K, a mean temperature of 220 K, a topographic variation, Δz, of 3 km, and a mean scale height of 10 km. These numbers correspond to a non-dimensional terrain variation of $Z = 0.3$ and a non-dimensional diurnal thermal range of about $\Theta = 0.18$. In combination, these yield a PΔDRSP between points A and B of just under 5.5% of the daily average value. The PΔDRSP of about 5% as modeled by WRF at $L_s = 160$ between the landing site (about 11%) and the plains to the east of Gale Crater (about 6%) is in good agreement with this estimate.

In principle, Eqn. (25) could be used to calculate the curves shown in Fig. 9b,d, and f. However, the equation was derived for conceptual clarity, not high-order predictive accuracy, which is better done with a numerical model directly or with the piecewise hydrostatic integration. Indeed, the non-dimensional numbers for the full Gale Crater example, used in the prior paragraph, are both somewhat larger than the 10% assumption used in deriving Eqns. (24 and 25) and thus a higher-order form would strictly be needed to reliably calculate the PΔDRSP for these kinds of settings.

Despite this, the trends predicted by Eqn. (25) are clearly correct. Larger diurnal air temperature cycles cause the gradients of the trajectories in Fig. 9b, d, and f to become shallower, corresponding to more change in PDRSP for a given range of elevation change. Note that these trajectories are not perfectly straight lines but rather gentle curves, as expected given the neglected higher order terms not included in the purely linear Eqn. (25). We also note that the analysis of contributions to the ΔDRSP (Eqns. (24 and 25)) assumes that lateral thermal contrasts can be ignored when comparing surface pressure at different elevations along the slope and that there is no temporal change in lateral thermal contrasts. While these assumptions constitute a good first approximation for the mesoscale Gale Crater region (Section 5), they limit the applicability of Eqns. 24 and 25 to a wider range of meso- and synoptic scale contexts. These equations are extended to treat cases of time-varying lateral thermal gradients in Part 3 of this sequence of papers.

6.5. The dominance of gravity and pressure gradient forces along slopes

Analysis of model output in Sections 4 and 5 demonstrates that the temporal and spatial variation of surface pressure over the Gale Crater region is that predicted from hydrostaticity based upon the model lowest layer air temperature and that local time (diurnal cycle) variations in air temperature dominate over lateral variations. While this empirically demonstrates the predominance of the along-slope gravity and lateral

pressure gradient forces, and while we note that the form of the along slope hydrostaticity (*e.g.,* Eqn. (11)) can be derived from first principles if this is assumed from the outset (*e.g.,* following Holton (1992) and rotating the coordinates), we can also approach the problem by starting from the full along-slope momentum equation and individually examining the size of each term to demonstrate why hydrostaticity is so closely maintained (*i.e.,* by conducting simple scale analysis; see, *e.g.,* Holton (1992) for a general introduction to scale analysis). We write the equations in terrain-following coordinates as this both approximates how the equations are written in the WRF model and allows us to closely parallel the formalism used by Blumsack et al., (1973). The sigma terrain-following coordinate is defined as the ratio of the air pressure at any given height and the corresponding surface pressure:

$$\sigma \equiv \frac{P}{P_s} \tag{26}$$

The full momentum equation along a slope (Eqn. (2.2) from Blumsack et al., (1973)) can be written:

$$\frac{D(uP_s)}{Dt} = fvP_s - \frac{\partial(RTP_s)}{\partial s} - \frac{\partial}{\partial \sigma}\left(\sigma \frac{\partial \phi}{\partial s} P_s\right) - P_s F_x \tag{27}$$

Where u is the along-slope wind, v is the across-slope wind, ϕ is the geopotential, f is the Coriolis parameter, and F_x is along-slope frictional acceleration. After expansion of the compound differentials, use of the hydrostatic relation along the sigma direction, and division by the surface pressure, Eqn. (27) can be written:

$$\frac{1}{P_s}\frac{D(uP_s)}{Dt} = fv - \frac{RT}{P_s}\frac{\partial P_s}{\partial s} - R\left(1 - \frac{1}{\sigma}\right)\frac{\partial T}{\partial s} - \frac{\partial \phi}{\partial s} - F_x \tag{28}$$

The geopotential gradient can be found from the slope angle, α, via the definition, $\sin\alpha \equiv \partial z/\partial s$, and of the geopotential, $\phi \equiv gz$, and thus:

$$\frac{\partial \phi}{\partial s} \equiv g \sin \alpha \tag{29}$$

For the scales of Gale Crater's topography, we can use values from MarsWRF output to estimate the relative size of terms in equation (28). We find that the forcing terms on its RHS, from left to right, are of order $10^{-4}, 10^{-1}, 10^{-3}, 10^{-1}, 10^{-5}$. From this scale analysis, the dominance of the slope projection of gravity and the compensating pressure gradient force is clear, and this is why lateral hydrostaticity is closely maintained along slopes at Gale-like scales. At mid- and high-latitudes, the Coriolis term (first term on RHS of Eqn. (28)) may be over an order of magnitude larger than given here but would still be much smaller than the along-slope gravity for mesoscale topographic relief of comparable magnitude to that at Gale Crater.

The Gale region has slopes of order 2.5° (about 5 km of relief over a lateral range of roughly 100 km). As the lateral scale of consideration increases by one or two orders of magnitude, the mean slopes decrease by a similar range of magnitude, meaning that $\sin\alpha$ and hence the penultimate term in Eqn. (28) decreases similarly. At the synoptic scale, the control of the force balance by along-slope hydrostaticity is thus less tight than at the mesoscale, and other dynamical systems can more readily influence the surface pressure evolution. This corresponds to the increased potential importance of neglected lateral thermal gradients, Coriolis deflection, and advection and convergence terms within coherent circulation systems, such as tides and traveling waves. Indeed, at synoptic length scales, the daily varying pressure distribution on Mars becomes dominated by the topographically-modified thermal tides while the seasonally varying distribution becomes strongly influenced by standing dynamical systems such as the tropical mean overturning circulation and the zonal jets, and by temporal changes in the latitudinal temperature structure which become important compared to temporal changes of the mean temperature. We revisit this topic at length in Part 3 of this sequence of papers.

6.6. Acceleration of the hydrostatic adjustment flow

The thermotopographically-induced hydrostatic adjustment flow acceleration is driven solely by the imbalance between the two dominant terms in Eqn. (28) (the second and fourth terms on the RHS). For conceptual simplicity, we neglect horizontal and vertical gradients within the wind field, allowing us to replace the total with the partial derivative to find the instantaneous flow acceleration:

$$\frac{\partial \overline{u}}{\partial t} = -\frac{1}{P_s}\frac{\partial P_s}{\partial s}R\overline{T} - g \sin \alpha \tag{30}$$

where we have also introduced a mass-weighted vertical averaging indicated by the overbar:

$$\overline{X} = \frac{\int_1^{\sigma_t} X(\sigma)d\sigma}{\int_1^{\sigma_t} d\sigma} \tag{31}$$

where X is the variable being averaged. The integration is performed upwards from the surface ($\sigma = 1$) to the value $\sigma = \sigma_t$ at the top of the flow or the layer of interest. Our consideration in previous Sections of the exact force balances along the slope within WRF can be viewed as evaluating Eqn. (31) over an interval from $\sigma = 1$ to $\sigma = 0.998333$ (*i.e.,* to the top of the lowest model layer, which was about 16.8 m above the surface for the model configuration used in most of this study – and which corresponds to vertical grid A discussed by Newman et al., (2017)). This is not likely to be the full depth of the hydrostatic adjustment flow, however, and we will return to the topic of the most appropriate evaluation of this depth in Part 2 of this paper sequence.

In the case of non-time-varying (constant) air temperature, the system would tend to a stationary state in which the two terms on the RHS of Eqn. (30) would balance. In this steady state, there is hydrostatic balance along the slope without any acceleration of the wind, and we recover Eqn. (13). Conversely, for a time-varying air temperature, if we take advantage of the fact that the full surface pressure gradient force may be separated into a hydostatically-balanced and a non-hydrostatically balanced component, then the pressure gradients are related by:

$$\frac{\partial \ln P_s}{\partial s} = \frac{\partial \ln P_h}{\partial s} + \frac{\partial \ln P_n}{\partial s} \tag{32}$$

As the winds are only accelerated by the nonhydrostatic pressure gradient force (and the hydrostatic portion exactly balances the g sin α term), Eqn. (30) becomes:

$$\frac{\partial \overline{u}}{\partial t} = -\frac{\partial \ln P_n}{\partial s}R\overline{T} = -\left[\frac{\partial \ln P_s}{\partial s} - \frac{\partial \ln P_h}{\partial s}\right]R\overline{T} \tag{33}$$

If we assume that radiative heating is much faster than the timescale for lateral mass redistribution, we can examine the sensitivity of Eqn. 33 to a small perturbation of the uniform air temperature. If the new temperature is equal to the prior state temperature, T_0, plus a perturbation, δT:

$$\overline{T}_1 = \overline{T}_0 + \delta T \tag{34}$$

then the new balanced hydrostatic state, to which the atmosphere is to be driven, is obtained from Eqn. (14) as:

$$\frac{\partial \ln P_h}{\partial s} = -\frac{g \sin \alpha}{R(\overline{T}_0 + \delta T)} \tag{35}$$

The as-yet still stationary atmosphere has not changed its lateral mass distribution, and thus the actual surface pressure distribution would initially remain in the prior hydrostatic state:

$$\frac{\partial \ln P_s}{\partial s} = \frac{-g \sin \alpha}{R\overline{T}_0} \tag{36}$$

We can now substitute Eqns. (35) and (36) into Eqn. (33) to yield:

$$\frac{\partial \overline{u}}{\partial t} = -\left[\frac{-g \sin \alpha}{R\overline{T}_0} - \frac{-g \sin \alpha}{R(\overline{T}_0 + \delta T)}\right](\overline{T}_0 + \delta T) = \frac{\delta T}{\overline{T}_0} g \sin \alpha \qquad (37)$$

Eqn. (37) tells us that the hydrostatic adjustment flow is accelerated uphill only when there is an increase in the spatial mean temperature, that the acceleration is proportional to the size of the temperature change relative to the initial state temperature, and that the flow is most strongly accelerated where the slope is steepest (*i.e.,* where the height separation between two fixed points along the slope is greatest).

Note that while the RHS of Eqn. (37) has the same form as a traditional 'buoyancy flow' (and also the same form as vertical wind acceleration within thermal convection if sinα is set to unity and u is replaced with w), the nature of the temperature perturbation is very different here. Specifically, here there is no spatial variation of δT, it simply represents the temporal change in spatial mean air temperature. This is different from the perturbation within the genetically defined buoyancy slope flow (and thermal convection), in which the spatial variation of the perturbation temperature is critical and where strictly it is assumed that there is no temporal change in the spatial mean air temperature (we expand much more completely on the distinctions between the thermotopographic flow types and their precise mechanical definitions in Part 2 of this sequence of papers). This highlights the critical importance of how buoyancy is defined. In the case of genetic slope flows and convection, buoyancy is very tightly defined as the force that acts on a parcel of air due to the density differences between the parcel and the surrounding air on the same isobaric level. In this way, traditional buoyancy is the force generated when a parcel of a given density is immersed in a fluid of a different density. Throughout this paper, we use buoyancy only in this sense.

However, it is also somewhat common to encounter "buoyancy" used in the literature defined in a less tightly genetic sense, as being the full or mean-state pressure gradient force directed along the vertical axis. In this case there is no sensible "immersion" of an air parcel and thus the nature of the force is very different from that of the true or genetic buoyancy. It is important in this light to always have a good understand which definition of buoyancy a given author is using. For example, previous work on Martian topographic flows by Blumsack et al., (1973) strictly refers to a long length-scale version of lateral hydrostatic adjustment and not to buoyancy slope flows as traditionally defined (*e.g.,* Mahrt, 1982; Pielke, 2002; Haiden, 2003). That the flow Blumsack et al., (1973) consider is the flow we refer to as the hydrostatic adjustment flow is demonstrated on page 68 of their paper: "The behavior of [the surface pressure] depends upon the rate of hydrostatic adjustment of the atmosphere in the horizontal. When the mean temperature varies diurnally there will be flow into and out of basins due to contraction and expansion of the atmosphere. We can show that the adjustment is rapid enough so that, averaged in the vertical, hydrostatic balance is closely maintained along typical Martian slopes. By this we mean that the force balance along the slope is between the component of gravity along the slope and the pressure gradient."

Returning to the quantification of the forces acting on a perturbed isothermal atmosphere, we can use Eqns. (35) and (36) in Eqn. (33) to find the nonhydrostatic pressure induced by the thermal perturbation and before mass redistribution has been accomplished:

$$\frac{\partial \ln P_n(t)}{\partial s} = \frac{\delta T g \sin \alpha}{R\overline{T}_0(\overline{T}_0 + \delta T)} \approx \frac{\delta T}{\overline{T}_0^2} \frac{g \sin \alpha}{R} \qquad (38)$$

The approximate form on the RHS of Eqn. (38) uses the assumption that δT ≪ T₀. The unbalanced nonhydrostatic pressure gradient (Eqn. (38)) will result in the lateral wind acceleration (Eqn. (37)) that initiates a mass redistributive flow. This flow will tend to evolve the mass from the distribution described in Eqn. (36) towards the new hydrostatic state described by Eqn. (35). From the conservation of mass in the absence of

sources or sinks, the surface pressure tendency equation may be derived as:

$$\frac{\partial P_s}{\partial t} = -\overline{u}\frac{\partial P_s}{\partial s} - P_s\frac{\partial \overline{u}}{\partial s} \qquad (39)$$

We can find a conservative estimate of the wind speeds required for the hydrostatic adjustment flow by assuming that the wind convergence provides no contribution (*i.e.,* that the second term on the RHS of Eqn. (39) is equal to zero). The rapidity of the adjustment and the required flow speeds can be estimated from Eqn. (39) based on the amount of mass that must be moved and the magnitude of the along-slope pressure gradients. From Fig. 1c we can estimate $\partial P_s/\partial t$ at the high or low elevation point on the slope (shown in blue or red, respectively) as roughly a 20–40 Pa change over 12 h. From either Fig. 7g or 7 h we find about a 5 Pa cumulative nonhydrostatic pressure difference between the plains and the Gale Crater trough, over a distance between these points of about 60 km. Depending on which values we use for the rate of pressure change, we estimate a required wind speed of between about 5 and 10 ms⁻¹ which as a rough estimate is reasonable compared to typical wind speeds generated within the Gale Crater system in both observations and mesoscale models (Newman et al., 2017). In reality, the MarsWRF model wind field suggests that the contribution from convergence/divergence is likely comparable to that of advection and thus that the required wind speeds are likely even lower, nearer 2.5–5 ms⁻¹.

6.7. Mass-driven hydrostatic adjustment flow

So far we have only mentioned the dominant, thermally driven hydrostatic adjustment flow. For completeness, however, it should be noted that a much smaller mass-driven hydrostatic adjustment flow will also be induced if there are large scale mass transports that uniformly import mass into or export mass out of the domain (*i.e.,* introducing negligible across-domain gradients). The major example of this for a mesoscale region on Mars is mass transport due to the (synoptic scale) thermal tide. Considering Fig. 10, if a uniform mass per unit area of air is removed from above both points A and B by the thermal tide, then this corresponds to removing a fixed amount of pressure, ΔP. In hydrostatic balance the surface pressures at points A and B are related to each other exponentially (Eqn. (10)), thus a uniform decrease of the surface pressure at both points disturbs the along-slope pressure gradient away from a state of hydrostaticity, and this again induces a hydrostatic adjustment flow, even in the idealized case of the air temperature remaining constant in time and isothermal in all three dimensions. This mass-driven flow would introduce an extra additive term to Eqns. (24) and (25) that would be related to the non-dimensional topographic height and the non-dimensional magnitude of the externally imposed (large-scale tidal) daily pressure variation. Removal of the tidal contribution from a numerical model of the flow over topography will also result in the removal of this contribution to the hydrostatic adjustment flow. Thus, for example, idealized limited-area simulations of Gale Crater by Tyler and Barnes (2015) that did not include a thermal tide will also not have generated a corresponding mass-driven hydrostatic adjustment flow.

We note that this "mass-driven" hydrostatic adjustment flow field is related to the perturbation motion describing how an otherwise homogeneous (large-scale) flow is modified as it passes over small-scale topography (see Section 2.2.1). The flow is thus larger when the Froude number is smaller, *i.e.,* it represents the degree to which the tide cannot achieve uniform, uninterrupted flow over terrain and thus the degree to which the terrain is non-dimensionally 'large'. As with the thermally induced hydrostatic adjustment flow, the perturbation flow field tends to zero as the ratio of the range of topographic height to the scale height tends to zero.

6.8. Lateral and vertical hydrostatic adjustment

It is important to note the distinction in the dominant mechanisms of *lateral* hydrostatic adjustment described in this paper and of *vertical* hydrostatic adjustment (*e.g.,* Bannon, 1995). While both are fundamentally driven by nonhydrostatic imbalances in the momentum equation (albeit separately in the along slope and along-the-gravity-vector directions, respectively – see Fig. 3) and both processes act to remove these imbalances, there are significant differences: 1. in the much greater force of gravity along the true vertical direction *vs.* along a shallow slope; 2. the much shorter distance and time scales over which vertical hydrostatic adjustment typically operates; 3., the relative importance of compressibility when short versus long time and length scales of forcing are imposed; and 4., the much greater importance of heat redistribution in the vertical adjustment problem.

The much shorter time and length scales of vertical hydrostatic adjustment mean that the compressibility of the fluid can be important. Rapid changes in temperature over short length scales tend to create gradients in pressure and density that break the assumption of incompressibility that works well for much of the atmosphere, and when examining the compressible adjustment to such sharp imposed disturbances, the solution inevitably involves consideration of the propagation of acoustic waves. Such waves govern the maximum rate of adjustment, are amenable to analytical study, and govern rapid injections of heat into the atmosphere such as occur in latent heating due to rainstorms (Bannon, 1995). The wave motions can significantly modify the vertical thermal, pressure, and density structure as all three fields mutually adjust towards a new balanced state. The resultant time-varying motion field thus generally displays considerable oscillatory behavior that can be seen, for example, in the evolving location of test particles within the fluid (Chagnon and Bannon, 2005a,b).

Ultimately, to achieve an end state of adjustment, net vertical mass redistribution is usually required. This net redistribution is that which is left after the transient, necessarily dissipative oscillatory motions have ceased. While the details of the transient motions may be important in many micro- and smaller mesoscale contexts (such as whether condensate forms in association with some of the motions, in determining the relative importance of thermal structure adjustment relative to net mass transport, and in generation of laterally-propagating disturbances), for most motions on larger meso- and synoptic scales, the net vertical motion can reasonably be diagnosed with a hydrostatic model from the differential horizontal convergence (and divergence) at different levels in the column and without need to consider the transient (acoustic wave) solutions. This corresponds to the time- and length scales of heating being considerably longer than the idealized, sharp forcing that is often used in acoustic wave modeling of adjustment (Chagnon and Bannon, 2005a,b). For example, although the transient solution is important for determining the evolution of the vertical mass distribution for individual plumes within convective storms, the transient response is far less significant when considering the adjustment to the average heating over the lateral scale of an entire mesoscale convective complex (Chagnon and Bannon, 2005a,b). For long length and time scales, it is conceptually just as useful to think of hydrostatic adjustment (both laterally and vertically) as being accomplished by the development of non-oscillatory vertical motion in response to the small offsets between gravity and vertical pressure gradient forces, and assuming negligible dynamical heating by the induced vertical motion. The diagnosed motion may be subtly different from the net motions that would be residual after the transients associated with the ensemble of plumes have abated (due to neglected heating), but the conceptualization of the vertical hydrostatic adjustment as associated with the net effect of the acoustic waves and with the development of "steady" vertical motion is qualitatively equivalent.

In consideration of the *lateral* hydrostatic adjustment problem over the lateral scales of Gale Crater and for the diurnal variation of heating, we only need to consider the net motions that result in the limit of the slow and nearly spatially continuous deposition (and removal) of heat (or

in the case described in Section 6.7, mass) over the daily cycle. Much like the extended areas and durations of heating examined by Chagnon and Bannon (2005a,b), we can assume that the transient, oscillatory behavior is small compared to the steady induced flow. This leads directly to the validity of the assumption used in consideration of mesoscale near surface flows (Haiden (2003) and in this paper) that the vertical, compressible adjustment is instantaneous (*i.e.,* that the atmosphere is always close to vertical hydrostatic balance, which is verified by the insensitivity of these simulations to running the model in hydrostatic or nonhydrostatic mode), and that lateral thermal adjustment by acoustic waves can be neglected. Consequently, for the lateral hydrostatic adjustment problem along varied terrain, we need only consider the slow net motions on scales of 10–100's of km and on timescales of hours.

This same reasoning also applies to flows on scales even larger than this. For example, the seasonal condensation flow results from the creation of atmospheric mass over the subliming polar cap and its destruction over the condensing cap. This process of atmospheric mass exchange will undoubtedly locally create acoustic waves, but we do not need to consider the transient, oscillatory motion in determining the required pole-to-pole condensation flow. Instead, the condensation flow can accurately be calculated by considering the development of flow in response to the lateral pressure gradients that develop from the widely spaced mass sources and sinks. In this way, the lateral hydrostatic adjustment flow discussed in this paper is more directly analogous to the pole-to-pole condensation flow than it is to the vertical hydrostatic adjustment of the atmosphere to rapid and intense moist convection, for example.

7. Summary, discussion, and relationship to prior and future work

The large diurnal range of surface pressure observed by the MSL REMS instrument is known to be due to the combined effects of the synoptic-scale thermal tide and mesoscale motions associated with the topographic and surface thermophysical variations. This understanding is based on the comparison of GCM (synoptic scale) and mesoscale model simulations from several different modeling groups and predates the arrival of MSL at Gale Crater (the "multi-model study" described in Sections 1 and 3). The separation of the tidal and non-tidal contributions is illustrated in this paper in Section 4.3 and Fig. 5 and requires a meaningful working definition of the thermal tide as a specific physical system, as detailed in Section 2.1. However, the question of the mechanism by which the mesoscale circulation amplifies the diurnal cycle at the landing site relative to that expected based purely upon the tide had not been comprehensively addressed prior to this work.

The topography comprising Gale Crater, Aeolis Mons, and the surrounding terrain contains many kilometers of vertical relief on lateral scales of 10–100 km. The resolution of this topographic relief in the mesoscale models is the reason why mesoscale simulations can adequately simulate the daily pressure cycle at the MSL landing site while lower-resolution GCM simulations cannot. This unambiguously points to the importance of mass-transportive mesoscale circulations forced over this terrain, but simply stating that the topography must somehow be responsible is not the same as providing a physical explanation. The reason for this is that many different, physically distinct types of thermotopographic flow mechanisms exist. For example, lateral flows that impinge upon complex terrain can generate locally induced circulation systems such as downslope wind storms (Section 2.2.1). In addition, cooling or heating of the air in layers parallel to the surface of sloping terrain can lead to buoyant flows, which are variously known as gravity flows, buoyancy slope flows, drainage flows, etc. (see Section 2.2.2.1), while lateral gradients in the heating of these layers can lead to slope-modified "sea breeze" circulations (Section 2.2.2.2).

In this paper, we primarily focus on the role of a fourth type of topographic flow associated with the lateral adjustment of the pressure over complex terrain to hydrostaticity as the mean air temperature is changed

(Section 2.2.2.3). The reason for this focus is that both Richardson et al., (2013) and Rafkin et al., (2016) have shown that the surface pressure distribution over the Gale Crater system and surrounding terrain remains close to a state of hydrostatic balance despite the very large diurnal cycle of air temperature and the consequent, similarly large change in the near surface scale height. This tendency for the surface pressure distribution to remain near a hydrostatic state evaluated using near surface air temperatures is shown in detail in Sections 4 and 5 of this paper.

Based upon the observation of the near hydrostaticity of the surface pressure distribution, in this paper we examined the nature of the flow that would be required to maintain a near balanced state. The restoring mechanism of balance can only be provided by lateral net mass movement and hence flow acceleration is required. Indeed, in the along slope momentum equation it is due to the difference between the projection of gravity along the slope and the along-slope pressure gradient force. For example, an increase in the mean air density due to a mean temperature decrease causes a downslope flow acceleration that redistributes the surface pressure so as to increase the lateral pressure gradient and restore a balance state (Section 6). During such a period of cooling, the actual surface pressure distribution will tend to have a deficit at low elevations and an excess at high elevations relative to a hydrostatic balance state at the same temperature. As such, a pressure gradient force exists that is directed down slope. This non-hydrostatic surface pressure gradient, which provides the force that drives the hydrostatic adjustment flow, is evident in the model output (Section 4 and Fig. 7g and h). A detailed discussion of distinction in forcing mechanisms between the hydrostatic adjustment flow and the other thermotopographic flows (Section 2.2.2), and the implications for how the various thermotopographic flows can influence the surface pressure evolution, requires a detailed and quantitative definition of the other thermotopographic flow components and is deferred to Part 2 of this series of papers.

The nature of the lateral hydrostatic adjustment is such that at low elevations it tends to increase the surface pressure during periods of cooling and tends to decrease it during periods of warming. At high elevations, the trend is reversed, while at intermediate elevations the surface pressure may remain unchanged. As such, the contribution of the hydrostatic adjustment flow to the full surface pressure variation is different for locations of different elevation within the region. Whether the location experiences an augmentation or diminution of the full surface pressure depends upon the surface elevation of the location, the local time-dependence of the air temperature variation, and the local-time variation of the thermo-tidal contribution (see Fig. 5 and discussion thereof). The hydrostatic adjustment flow and the thermal tide are physically distinct processes and are only linked through their differing dependence upon forcing ultimately by the diurnal cycle of solar heating.

The thermal effects of the hydrostatic adjustment flow and the need to develop a pressure gradient force to drive the flow both lead to the actual daily surface pressure cycle at low elevation sites such as that of MSL landing being smaller than if perfect hydrostaticity were always maintained. Since the downhill flow occurs during the cooling portion of the daily cycle, and downhill adiabatic heating tends to warm the air, and vice versa, the thermal effects of the hydrostatic adjustment flow tend to reduce the daily amplitude of temperature, and thus the thermal effect of the hydrostatic adjustment flow is to slightly damp the daily pressure cycle. Further, since a pressure gradient force is required in order to drive the hydrostatic adjustment flow, the deficit of surface pressure at low elevation during the cooling portion of the day that drives the convergent flow means that the (real) non-equilibrium surface pressure is never as high as the extremum instantaneous balance state. Similarly, during the warmest part of the day, the actual surface pressure is never as low as that for instantaneous balance state at the same temperature. As such, the dynamical necessity of driving the hydrostatic adjustment flow means that hydrostaticity is never fully achieved and the diurnal range of pressure is thus smaller than perfect hydrostaticity would predict (Section 5 and Fig. 7g and h).

The time and length scales of heating over the topography are such

that the compressibility of the atmosphere is not important and the flow is likely not significantly influenced by transient, oscillatory motions. As such, the proposed lateral hydrostatic adjustment process is likely better conceptualized as a net flow rather than as an acoustic wave adjustment. This is different from how vertical hydrostatic adjustment is often considered and more akin to how we conceptualize the global condensation flow.

The hydrostatic adjustment flow and its explanation of the surface pressure evolution at Gale Crater described in this paper is consistent with prior discussion by Richardson et al., (2013) and (neglecting differences of terminology, see Section 3) Rafkin et al., (2016). This paper, expands upon these studies by providing a far more detailed analysis of the surface pressure evolution over the Gale Crater region and a detailed proposal as to the nature, mechanism, and consequences of the adjustment flow. The present paper differs from Tyler and Barnes (2013; 2015) in providing a concrete suggestion as to the nature of the flow responsible for the surface pressure redistribution over the Gale Crater topography. We also differ in the sense of strongly discouraging the usage of the "crater circulation" terminology: such terminology does not advance a meaningful mechanism for the mesoscale augmentation of the pressure cycle at the MSL landing site; and it implies a genetic dependence upon the specific structure of craters (as opposed to volcanoes, or mountains, or channels, etc.) that is not demonstrated by Tyler and Barnes (2013; 2015). Indeed, the hydrostatic adjustment flow is described in this paper without reference to the shape or nature of the complex terrain, which suggests that it is independent of these details. This issue is revisited in Part 3 of this sequence of papers.

Similarly, the limiting lateral scale of the hydrostatic adjustment flow has not been discussed in this paper. The rebalancing has been described for a mesoscale domain with reference to locations that are above or below the domain average elevation, but the question of what defines the average elevation has not been examined. For example, is this the equivalent of the mean "sea level" (or more appropriately for Mars, the MOLA datum)? Or is it the average over a domain circumscribed by a specific configuration of topography or by a limiting range of motion on diurnal timescales? This important question is deferred to Parts 2 and 3 of this study.

The scale and nature of the rebalancing flow is also important for determining how useful the PDRSP is for examining the influence of topography across the Martian surface. The PDRSP is a convolved diagnostic that includes the effects of both the local circulation and the thermotidal circulation. Over scales of the Gale Crater system we can consider the latter to be horizontally uniform, but this is clearly not the case over the whole planet (Wilson and Hamilton, 1996; Guzewich et al., 2016). At latitudes where Coriolis effects and thermal gradients become more important, the simple picture of the local flow as being dominated by the hydrostatic adjustment flow alone will also potentially break down. Similarly, the local time phasing of the thermal tide and the relative importance of the semi-diurnal and diurnal contributions will change with location. As such, the general value of PDRSP is probably much more limited than suggested by Tyler and Barnes (2015). Instead, the contribution due to the thermal tide will need to be properly removed through a form of filtering or forward modeling, and the behavior of the non-tidal flow will need to be examined separately. The variation of the non-tidal contribution is far more diagnostically useful for examination of the local mass-redistributive flow than the full PDRSP and this will again be addressed in detail in Part 3.

Appendix A. The relationship between surface pressure and the total column atmospheric mass at any point on the surface

Conditions in the Martian atmosphere mean that we can make certain basic assumptions that simplify the application of physical laws. These simplifications allow us to determine a very simple relationship between the surface pressure at any point on the planet and the column-integrated mass of atmosphere above that point. Specifically, the surface pressure is equal to the column-integrated mass of the atmosphere per unit surface area multiplied by gravity for almost all situations on Mars.

We first assume that the atmosphere is a continuum. This means that we can treat the atmosphere as a fluid and ignore the fact that it is composed of particles (primarily CO_2 molecules). This assumption relies on the mean free path of collisions being far smaller than the scale height and it allows us to define fluid quantities such as the pressure and to use a convenient equation of state. For Mars, we typically use the ideal gas law of form:

$$P = \rho RT \tag{A1}$$

where P is the pressure, ρ is the density, R is the specific gas constant (which is the ideal gas constant divided by the molar mass) and T is the temperature.

Second, we assume that the bulk global atmosphere is neither rapidly escaping nor collapsing. The assumption can be summarized as stating that over the whole column, $dw/dt \sim 0$, where w is the vertical wind speed. This means that we can write a global mean vertical momentum equation wherein the dominant balance is between the gravitational attraction of the atmosphere down onto the planet's surface and the pressure gradient force of the atmosphere outwards towards the vacuum of space. This is the hydrostatic balance and can be written in the form:

$$\frac{\partial P}{\partial z} = -\rho g \tag{A2}$$

where z is the radial distance upwards from the surface and g is the acceleration due to gravity. It should be noted that for equation (A2) to be invalid due to atmospheric escape, the vertical acceleration of the outflow would need to be comparable to that of gravity throughout the column, and the flow would need truly to be escaping such that the acceleration could not integrate to zero through the full depth of the atmosphere. An example of such a rapidly escaping continuum atmosphere would be a cometary coma. It should also be noted that the rate of CO_2 condensation and sublimation at the Martian seasonal poles is sufficiently slow such that the Martian lower atmosphere is never escaping or collapsing by this definition and that hydrostatic balance can usefully be defined for Mars.

Third, we assume that we are considering a thin-shell atmosphere. This means that the characteristic depth of the atmosphere (such as the scale height) is small compared to the radius of the planet. This allows us to treat acceleration due to gravity as being constant throughout the depth of the lower atmosphere. Between the surface and 100 km, this introduces a roughly 5% error in the estimation of g for Mars, and results in a much smaller error in the estimation of surface pressure as the mass is preponderantly concentrated within the lowest 10 km or so of the column. The utility of this assumption is that the integral of the right hand side of equation (A2) over depth now produces the same value irrespective of how the mass is distributed with height within the column. This integral yields:

$$\int \partial P = -g \int \rho \partial z \tag{A3}$$

The density integrated over the depth of the atmosphere is simply the mass per unit area of the atmospheric column, and hence we have the useful definition of the surface pressure as being the mass per unit area multiplied by the constant acceleration due to gravity. Generally, then, we can write:

$$P_{SURF} = \frac{M}{A} g \tag{A4}$$

where M/A is the mass per unit area of the column.

Equation (A4) has important implications for how the surface pressure can change at any given location on Mars. Ignoring the polar regions, where CO_2 gas can be "created" and "destroyed" by conversion from/to CO_2 ice, and also ignoring atmospheric loss processes at the top of the atmosphere (which are vanishingly slow on meteorological timescales), the law of conservation of mass means that the surface pressure can only be changed by lateral net advection of mass into or out of the column. As such, any change in surface pressure must by definition be due to a net convergent or divergent circulation. Examples of convergent and/or divergent circulations include most micro-scale and all meso- and synoptic scale meteorological systems that include a surface pressure signature, from the relative highs and lows in small-scale boundary layer convection cells and dust devils, to those in extra-tropical cyclones and in the patterns of the global scale thermal tides. A statement that the surface pressure at any given (non-polar) location is changing is thus identically equal to the statement that a convergent/divergent circulation is at work. The only exception to this rule is provided if the net vertical acceleration very close to the surface is comparable to that of gravity. Shock waves from detonations or microburst currents within rain storms can yield non-hydrostatic perturbations of the surface pressure. Such perturbations tend to be on very short length and timescales as the driving force to return to hydrostaticity is very strong.

That the surface pressure for almost all meteorological systems is defined as the mass per unit area multiplied by gravity means that the thermal structure above the surface (and equivalently the vertical distribution of mass in the column) does not directly influence the surface pressure. No matter

how we change the balanced-state thermal structure and the vertical distribution of mass within the column, the surface pressure is unmodified. The only influence of thermal structure on surface pressure is secondary and specifically through the forcing of net lateral motions. Note that even strong nonhydrostatic vertical accelerations within the interior of the fluid column do not influence the surface pressure unless there is mass-weighted, column-integrated net vertical acceleration.

Note that the relationship between surface pressure and mass per unit area above the surface applies when thinking about the surface pressure from any perspective. For example, when raindrops or ice particles initially form in the atmosphere, the surface pressure will decrease by the amount of mass converted to condensate. The affect of the mass decrease on the surface pressure takes some time to register as the pressure adjustment is accomplished by acoustic propagation from the site of condensate particle formation. The mass drop of the atmosphere only occurs because as the condensate particles form they initially fall at a rate unbalanced (or unsupported) by the atmosphere. As the particle speed increases, atmospheric drag on the particles increases and at terminal velocity the particle weight is supported by the column. At this point, the surface pressure returns to the value before the condensate particle formation. The column surface pressure only decreases again when the particles sediment to the surface. The influence of precipitation particles on surface pressure is described in much greater detail by Spengler et al., (2011). Similarly, the mass of a plane flying in level flight overhead increases the surface pressure.

Finally, if the ideal gas law (the equation of state) is reapplied at the surface, we obtain $P_{SURF} = \rho R T_{AIR}$, where P_{SURF} is the surface pressure, ρ is the density of the near surface air, R is the specific gas constant and T_{AIR} is the near surface air temperature. This relationship allows some conceptual separation of the physical causes of changes in the three variables. P_{SURF} can only be changed by net lateral advection of mass. Irrespective of how the air temperature is changed (so long as it is changed slowly), the surface pressure will only be modified by net mass transport. In the absence of net advection of mass, slow changes in air temperature only change the local air density. T_{AIR} can be modified by a wide range of process, from radiative heating to convection and dynamical (adiabatic) heating and thermal advection. For the Martian near-surface atmosphere, local control of air temperature due to convective and radiative coupling to the surface is very strong, with ground temperatures conversely not being strongly influenced by sensible or radiative exchange with the atmosphere. Thus to a good first approximation, one can consider P_{SURF} to be driven by dynamical processes, T_{AIR} by local radiative-convective processes, and the density to be a diagnostic constrained to be whatever is needed to satisfy the equation of state given P_{SURF} and T_{AIR}.

The foregoing assumes that the atmosphere has a free upper boundary such that the only external forces acting on the fluid are gravity operating throughout the body of the fluid and the reaction force of the ground operating at the lower boundary of the fluid. The atmosphere is assumed free to extend vertically *ad infinitum*. If this were not true, a case that might correspond to placing an arbitrary rigid top or fixed ceiling at the upper boundary, then an additional reaction force may be generated at the domain top. The size and sign of this reaction force depends upon the height of the top above the ground relative to the scale height and the distribution of the air within the capped column relative to that which would occur for the same mass of gas at the same temperature in a free atmosphere. The simplest consideration would be to imaging placing a ceiling into an initially equilibrated atmosphere and then consider the effect of heating the atmosphere. Since the mean density of the atmosphere can no longer change (the column mass and the column depth are now fixed), a temperature increase can only cause a change in surface pressure. Thus, the surface pressure now corresponds to the sum of the column mass plus the pressure corresponding to the extra reaction force now generated from the trapping of the warmed air against the domain rigid lid. This somewhat artificial effect of imposing a lid is consequential for some numerical models (those that use height-based vertical coordinates) and also for consideration of how fluids move beneath strong capping inversions.

Appendix B. MarsWRF model description

The MarsWRF model used in this study is based on the NCAR WRF model (Skamarock and Klemp, 2008; Powers et al., 2017) version 3.3.1 but includes elements (such as the boundary layer schemes) updated to v3.8.1. The conversion of WRF for planetary and Martian use has been described by Richardson et al. (2007) and Toigo et al. (2012). As used in this study, the model provides a fully compressible and nonhydrostatic simulation of atmospheric motions on a finite difference, grid point mesh. The model uses a terrain-following modified sigma ("eta") coordinate in the vertical. The terrain information is generated from the final MOLA MEGDR laser altimeter map product at $1/128^{th}$ of a degree resolution (Smith et al., 2003). Over the region of Gale Crater, the MOLA topography is overlain with a Digital Terrain Map derived from the Mars Express High Resolution Stereo Camera (HRSC) (Gwinner et al., 2016). The merged topography is averaged onto the spatial grids at the relevant resolution.

MarsWRF uses a regular gridded horizontal domain that can be projected conformally or unconformally onto the sphere (or a portion thereof). As such, it can be used to represent global and a variety of limited-area domains. The latter allows for a wide range of forced-boundary condition and idealized simulations. It also allows nesting of higher resolution domains within lower resolution domains, and for this to be done recursively to an arbitrary number of levels. Unlike other Mars mesoscale models, MarsWRF is capable both of generating its own global model state (*i.e.,* can be run as a GCM) to force limited area domains, but also of allowing these domains to be run interactively within the global domain ("two-way nesting"). In the nesting processes, boundary conditions for each nest are provided from extrapolation of conditions from the appropriate times and locations in the parent domain. The boundary conditions from the parent are applied to a daughter nest over the three grid points at the outermost edge of the nest domain. The "parent" is simply the larger scale domain within which the nest (the "daughter") is embedded. For successive levels of nesting, a given nested domain may be both a daughter forced by a larger-scale, lower resolution domain, and the parent of a smaller-scale, higher resolution domain. The two-way nature of the nesting is completed when the output generated by the higher-resolution daughter domain is averaged and replaces the prognostic fields generated for the nested domain area within its parent. As such, information flows in both directions from large-to-small and small-to-large scale across the domains and from the global mother domain down to (and back up from) the nth recursively two-way nested domain. A factor of 3 increase in resolution is typically used from nest to embedded nest.

In this study, we show output from two main MarsWRF simulation types (Table 1). The first simulation type (referred to as the "WithNests" case) was undertaken with a global parent domain (domain 1) that had grid points evenly distributed in increments of $2°$ in latitude and longitude. Three levels of nesting centered on the Gale Crater Curiosity landing site were used. Each nest was comprised of a square domain of 120 grid points on a side. Each successive nest had decreased grid spacing (increased resolution) by a factor of 3 relative to its parent. The timestep used inside each nested domain was also a factor of 3 smaller than its parent. At three subsequent levels of zooming, the innermost domain (domain 4) had a grid spacing of roughly $0.074°$. This corresponds to a latitudinal grid spacing of roughly 4.4 km. WithNests output from domains 1 and 4 are used in this study. The second simulation we show was identical to the global domain from the first simulation; the only difference being that no embedded nests were used. We refer to this simulation as "WithOutNests". In this case, MarsWRF was simply run as a $2°$ GCM.

The standard domains of the "WithNests" and "WithOutNests" model use the same vertical grid, with 40 uniform mass layers above 150 m and 3 lower layers below 150 m that progressively halve in thickness such that the lowest layer center is roughly 8 m above the surface. The model top is placed at 120 km, but with a very thick upper layer. We refer to this as "Vert Grid 410", as this mostly closely matches the vertical grid selection name used within MarsWRF model code. It corresponds to Grid A in Newman et al., (2017). The global domain employs a 30s time step, with the time step decreasing by a factor of 3 for each domain, such that the 4.4 km domain uses a roughly 1s time step. Sensitivity tests for the WithNests and WithOutNests have been completed with a range of vertical grids employing up to 72 layers.

The model uses a 15-layer implicit subsurface heat diffusion parameterization that simulates the subsurface thermal profile to several seasonal skin depths. The initial temperature is determined from a prior multi-annual simulation. The surface energy balance includes treatment of CO_2 ice condensation/sublimation and the resultant removal/addition of mass to the atmosphere. The parameters for the seasonal cap properties were determined for the model following the fitting approach of Guo et al. (2009) and the global domain was spun-up for 5 Martian years in order to assure a good steady state seasonal CO_2 cycle (nested simulations are undertaken only after the global model has been fully spun-up). The surface layer exchange and the planetary boundary layer (PBL) mixing of heat and momentum are represented using the Yonseu University (YSU) PBL scheme (Hong et al., 2006) (as revised Jimenez and Dudiha (2012) and Jimenez et al. (2012)) and using a roughness length scale map based on MOLA intra-shot variance (Garvin et al., 1999). In some simulations, the non-local, first order closure YSU scheme is replaced with the local, 1.5th order closure Mellor-Yamada-Janjić (MYJ) scheme (Janjić, 1994). We note here only in passing that the concern raised regarding the validity of PBL schemes used in all extant Mars mesoscale models to represent daytime convection when the grid-spacing is smaller than about 10–30 km applies to this study due to the need to resolve consequential variations in topography on lateral scales of only a few kilometers (this is the "terra incognita" or "grey zone" problem, Wyngaard (2004), Zhou et al., (2014) and for Mars, Newman et al. (2017)). Radiative heating of the surface and atmosphere uses the "k-distribution model" (KDM) radiative transfer scheme described by Mischna et al., (2012). Optical properties for dust follow Wolff et al., (2006). The distribution of dust optical depth spatially and temporally for the purposes of radiative heating follows a Mars Global Surveyor (MGS) scenario from the Mars Climate Database (Montmessin et al., 2004). Heating of the surface takes into account the surface albedo and thermal inertia (Putzig and Mellon, 2007), the topographic slope angle and orientation, and any shadowing of the direct solar beam by topography.

A point of potential confusion when discussing models relates to the ability of terrain-following coordinate models such as MarsWRF to represent hydrostatic balance along slopes. Such models by definition have a vertical direction within which gravity is represented as a part of the (vertical) momentum equation, either prognostically or within the diagnostic hydrostatic relation. This vertical axis is treated as being perpendicular to the "horizontal" axes, which are really directed along the surfaces of the terrain-following coordinate. While gravity does not directly appear in the "horizontal" momentum equations, it does appear through the lateral variation of the terrain geopotential. As such, models with terrain-following coordinates are able to represent hydrostatic balance forces along moderate slopes even though the along-slope direction is nominally orthogonal to the model vertical axis.

Finally, all the simulations undertaken in the body of this study use the nonhydrostatic option for the vertical (the along-the-gravity-vector direction) momentum equation. Incomplete compressibility was found to be problematic for earlier versions of the nonhydrostatic Mars RAMS model (Michaels et al., 2006) and for MM5 (Tyler and Barnes, 2005). WRF has from the outset used a fully compressible approach and has never suffered from these concerns (Skamarock and Klemp, 2008). As expected, testing of otherwise identical MarsWRF runs conducted with the hydrostatic *vs.* the non-hydrostatic option (a run-time choice for WRF) yields results at the scales of importance in this study (and for the atmospheric quantities of interest) that are effectively identical.

Appendix C. Supplementary data

Supplementary data related to this article can be found at https://doi.org/10.1016/j.pss.2018.07.003.

References

Baines, Peter G., 1998. Topographic Effects in Stratified Flows. Cambridge University Press.

Bannon, P.R., 1995. Hydrostatic adjustment: lamb's problem. J. Atmos. Sci. 52, 1743–1752.

Barnes, J.R., 1980. Time spectral analysis of midlatitude disturbances in the martian atmosphere. J. Atmos. Sci. 37, 2002–2015.

Blumsack, S.L., Gierasch, P.J., Wessel, W.R., 1973. An analytical and numerical study of the martian planetary boundary layer over slopes. J. Atmos. Sci. 30, 66–82.

Chagnon, J.M., Bannon, P.R., 2005a. Wave response during hydrostatic and geostrophic adjustment. Part I: transient dynamics. J. Atmos. Sci. 62, 1311–1329.

Chagnon, J.M., Bannon, P.R., 2005b. Wave response during hydrostatic and geostrophic adjustment. Part II: potential vorticity conservation and energy partitioning. J. Atmos. Sci. 62, 1330–1345.

Durran, D.R., 2003. Encyclopedia of Atmospheric Sciences. Elsevier Science Ltd, pp. 644–650, 2003.

Fenton, L.K., Richardson, M.I., 2001. Martian surface winds: insensitivity to orbital changes and implications for aeolian processes. J. Geophys. Res. 106 (E12), 32885–32902. https://doi.org/10.1029/2000JE001407.

Garvin, J.B., Frawley, J.J., Abshire, J.B., 1999. Vertical roughness of Mars from the Mars orbital laser altimeter. Geophys. Res. Lett. 26, 381–384.

Golombek, M.P., et al., 2003. Selection of the Mars exploration rover landing sites. J. Geophys. Res. 108, 8072. https://doi.org/10.1029/2003JE002074. E12.

Gómez-Elvira, Javier, Armiens, Carlos, Carrasco, Isaías, Genzer, Maria, Gómez, Felipe, Haberle, Robert, Hamilton, Victoria E., et al., 2014. Curiosity's rover environmental monitoring station: Overview of the first 100 sols. J. Geophys. Res.: Planets 119 (7), 1680–1688.

Guzewich, S.D., Newman, C.E., de la Torre Juárez, M., Wilson, R.J., Lemmon, M., Smith, M.D., Kahanpää, H., Harri, A.M., 2016. Atmospheric Tides in Gale Crater, Mars. Icarus, vol. 268, pp. 37–49.

Guo, X., Lawson, W.G., Richardson, M.I., Toigo, A.D., 2009. Fitting the Viking Lander surface pressure cycle with a Mars general circulation model. J. Geophys. Res. 114, E07006. https://doi.org/10.1029/2008JE003302.

Gwinner, K., Jaumann, R., Hauber, E., Hoffmann, H., Heipke, C., Oberst, J., Neukum, G., et al., 2016. The High Resolution Stereo Camera (HRSC) of Mars Express and its approach to science analysis and mapping for Mars and its satellites. Planet. Space Sci. 126, 93–138.

Haberle, R.M., Leovy, C.B., Pollack, J.B., 1982. Some effects of global dust storms on the atmospheric circulation of Mars. Icarus 50, 322–367.

Haiden, T., 2003. On the pressure field in the slope wind layer. J. Atmos. Sci. 60, 1632–1635. https://doi.org/10.1175/1520-0469(2003)60<1632:OTPFIT>2.0.CO;2.

Harri, A.-M., et al., 2014. Pressure observations by the Curiosity rover: initial results. J. Geophys. Res. Planets 119. https://doi.org/10.1002/2013JE004423.

Hess, S.L., Henry, R.M., Leovy, C.B., Ryan, J.A., Tillman, J.E., 1977. Meteorological results from the surface of Mars: viking 1 and 2. J. Geophys. Res. 82 (28), 4559–4574. https://doi.org/10.1029/JS082i028p04559.

Hong, Song-You, Noh, Yign, Dudhia, Jimy, 2006. A new vertical diffusion package with an explicit treatment of entrainment processes. Mon. Wea. Rev. 134 (9), 2318–2341.

Holton, J.R., 1992. An Introduction to Dynamical Meteorology, third ed. Academic Press.

Hourdin, F., Le Van, P., Forget, F., Talagrand, O., 1993. Meteorological variability and the annual surface pressure cycle on Mars. J. Atmos. Sci. 50, 3625–3640.

Janjić, Z.I., 1994. The step-mountain eta coordinate model: further developments of the convection, viscous sublayer, and turbulence closure schemes. Mon. Wea. Rev. 122, 927–945. https://doi.org/10.1175/1520-0493(1994)122<0927:TSMECM>2.0.CO;2.

Jimenez, P., Dudhia, J., Gonzalex-Rouco, J.F., Navarro, J., Montavex, J.P., Garcia-Bustamante, E., 2012. A revised scheme for the WRF surface layer formulation. Mon. Weather Rev. 140, 898–918.

Jimenez, P., Dudhia, J., 2012. Improving the representation of resolved and unresolved topographic effects on surface wind in the WRF model. J. Appl. Meteor. Climatol. 51, 300–316.

Leovy, C.B., Zurek, R.W., 1979. Thermal tides and martian dust storms: direct evidence for coupling. J. Geophys. Res. 84 (B6), 2956–2968. https://doi.org/10.1029/JB084iB06p02956.

Mahrt, L., 1982. Momentum balance of gravity flows. J. Atmos. Sci. 39, 2701–2711.

Martínez, G.M., Newman, C.N., De Vicente-Retortillo, A., et al., 2017. Space Sci. Rev. 212, 295. https://doi.org/10.1007/s11214-017-0360-x.

Michaels, T.I., Colaprete, A., Rafkin, S.C.R., 2006. Significant vertical water transport by mountain-induced circulations on Mars. Geophys. Res. Lett. 33, L16201 https://doi.org/10.1029/2006GL026562.

Miller, S.T.K., Keim, B.D., Talbot, R.W., Mao, H., 2003. Sea breeze: structure, forecasting and impacts. Rev. Geophys. 41, 1/1–131.

Mischna, M.A., Lee, C., Richardson, M., 2012. Development of a fast, accurate radiative transfer model for the Martian atmosphere, past and present. J. Geophys. Res. 117, E10009 https://doi.org/10.1029/2012JE004110.

Montmessin, F., Forget, F., Rannou, P., Cabane, M., Haberle, R.M., 2004. Origin and role of water ice clouds in the martian water cycle as inferred from a general circulation model. J. Geophys. Res. 109, E10004 https://doi.org/10.1029/2004JE002284.

Newman, C.E., Gómez-Elvira, J., Marin, M., Navarro, S., Torres, J., Richardson, M.I., Battalio, J.M., Guzewich, S.D., Sullivan, R., de la Torre, M., Vasavada, A.R., Bridges, N.T., 2017. Winds measured by REMS during MSL's Bagnold Dunes Campaign & comparison with numerical modeling using MarsWRF. Icarus 291, 203–231. https://doi.org/10.1016/j.icarus.2016.12.016.

Pielke, R.A., 2002. Mesoscale Meteorological Modeling. Academic Press, pp. 153–158.

Powers, J.G., et al., 2017. The weather Research and forecasting model: overview, system efforts, and future directions. Bull. Am. Meteorol. Soc. 98 (8), 1717–1737. https://doi.org/10.1175/bams-d-15-00308.1.

Putzig, N.E., Mellon, M.T., 2007. Apparent thermal inertia and the surface heterogeneity of Mars. Icarus 191, 68–94. https://doi.org/10.1016/j.icarus.2007.05.013.

Rafkin, S.C.R., et al., 2016. The meteorology of Gale Crater as determined from rover environmental monitoring station observations and numerical modeling. PartII: interpretation. Icarus. https://doi.org/10.1016/j.icarus.2016.01.031.

Rafkin, S., Haberle, R., Michaels, T., 2001. The Mars regional atmospheric modeling system: model description and selected simulations. Icarus 151, 228–256.

Richardson, M.I., Heavens, N.G., Mischna, M.A., Newman, C.E., Wilson, R., MSL Science Team, 2013. Why the Diurnal Pressure Variation at Curiosity is so Large. In: American Geophysical Union, Fall Meeting 2013 abstract #P41C-1925.

Richardson, M.I., Toigo, A.D., Newman, C.E., 2007. PlanetWRF: a general purpose, local to global numerical model for planetary atmo- spheric and climate dynamics. J. Geophys. Res. 112, E09001 https://doi.org/10.1029/2006JE002825.

Schofield, J.T., Barnes, J.R., Crisp, D., Haberle, R.M., Magalhaes, J.A., Murphy, J.R., Seiff, A., Larsen, S., Wilson, G., 1997. The Mars pathfinder atmospheric structure investigation/meteorology (ASI/MET) experiment. Science 278, 1752–1758.

Skamarock, W.C., Klemp, J.B., 2008. A time-split nonhydrostatic atmospheric model for weather and forecasting applications. J. Comp. Physiol. 227, 3465–3485. https://doi.org/10.1016/j.jcp.2007.01.037.

Smith, D., Neumann, G., Arvidson, R.E., Guinness, E.A., Slavney, S., 2003. Mars Global Surveyor Laser Altimeter Mission Experiment Gridded Data Record. NASA Planetary Data System. MGS-M-MOLA-5-MEGDR-L3-V1.0.

Spengler, T., Egger, J., Garner, S.T., 2011. How does rain affect surface pressure in a one-dimensional framework? J. Atmos. Sci. 68, 347–360. https://doi.org/10.1175/2010JAS3582.1.

Spiga, Aymeric, Forget, Francois, Madeleine, Jean-Baptiste, et al., 2011. The impact of martian mesoscale winds on surface temperature and on the determination of thermal inertia. Icarus 212 (2), 504–519. https://doi.org/10.1016/j.icarus.2011.02.001.

Toigo, A.D., Richardson, M.I., 2002. A mesoscale model for the Martian atmosphere. J. Geophys. Res. 107, 5049. https://doi.org/10.1029/2000JE001489.

Toigo, A.D., Richardson, M.I., 2003. Meteorology of proposed Mars exploration rover landing sites. J. Geophys. Res. 108 (E12), 8092. https://doi.org/10.1029/2003JE002064.

Toigo, A.D., Lee, C., Newman, E., Richardson, M.I., 2012. The impact of resolution on the dynamics of the martian global atmosphere: varying resolution studies with the MarsWRF GCM. Icarus 221 (1), 276–288. https://doi.org/10.1016/j.icarus.2012.07.02. ISSN: 00191035.

Tyler Jr., D., Barnes, J.R., Haberle, R.M., 2002. Simulation of surface meteorology at the Pathfinder and VL1 sites using a Mars mesoscale model. J. Geophys. Res. 107 (E4) https://doi.org/10.1029/2001JE001618.

Tyler, D., Barnes, J.R., 2005. A mesoscale model study of summertime atmospheric circulations in the North Polar Region of Mars. J. Geophys. Res. 110, E06007 https://doi.org/10.1029/2004JE002356.

Tyler, D., Barnes, J.R., 2013. Mesoscale modeling of the circulation in the Gale Crater region: an investigation into the complex forcing of convective boundary layer depths. MARS 8, 58–77. https://doi.org/10.1555/mars.2013.0003.

Tyler, D., Barnes, J.R., 2015. Convergent crater circulations on Mars: influence on the surface pressure cycle and the depth of the convective boundary layer. Geophys. Res. Lett. 42, 7343–7350. https://doi.org/10.1002/2015GL064957.

Vasavada, A.R., et al., 2012. Assessment of environments for Mars Science Laboratory entry, descent, and surface operations. Space Sci. Rev. 170, 793–835.

Wang, H., Richardson, M.I., Wilson, R.J., Ingersoll, A.P., Toigo, A.D., Zurek, R.W., 2003. Cyclones, tides, and the origin of a cross-equatorial dust storm on Mars. Geophys. Res. Lett. 30 (9), 1488. https://doi.org/10.1029/2002GL016828.

Wang, H., Zurek, R.W., Richardson, M.I., 2005. Relationship between frontal dust storms and transient eddy activity in the northern hemisphere of Mars as observed by Mars Global Surveyor. J. Geophys. Res. 110, E07005. https://doi.org/10.1029/2005JE002423.

Wilson, R.J., Hamilton, K., 1996. Comprehensive model simulation of thermal tides in the martian atmosphere. J. Atmos. Sci. 53, 1290–1326.

Wilson, R.J., Richardson, M.I., 2000. The Martian atmosphere during the Viking mission, 1. Infrared measurements of atmospheric temperatures revisited. Icarus 145, 555–579.

Wolff, M.J., et al., 2006. Constraints on dust aerosols from the Mars exploration rovers using MGS overflights and mini-TES. J. Geophys. Res. 111, E12S17 https://doi.org/10.1029/2006JE002786.

Wyngaard, J.C., 2004. Toward numerical modeling in the "terra incognita.''. J. Atmos. Sci. 61, 1816–1826.

Ye, Z.J., Segal, M., Pielke, R.A., 1987. Effects of atmospheric thermal stability and slope steepness on the development of daytime thermally induced upslope flow. J. Atmos. Sci. 44, 3341–3354.

Ye, Z.1., Segal, M., Pielke, R.A., 1990. A comparative study of daytime thermally induced upslope flow on Mars and Earth. J. Atmos. Sci. 47, 612–628.

Zhou, B., Simon, J.S., Chow, F.K., 2014. The convective boundary layer in the Terra Incognita. J. Atmos. Sci. 71, 2545–2563.

Zurek, R.W., 1976. Diurnal tide in the Martian atmosphere. J. Atmos. Sci. 33, 321–337.